Modification of the Liquefaction Potential Index to Consider the Topography in Christchurch, New Zealand

Vahid Rashidian[1]

Ph.D. Student, Civil and Environmental Engineering Department, Tufts University
200 College Avenue, Medford, MA 02143, U.S.A.
E-mail: vahid.rashidian@tufts.edu

Daniel T.Gillins, Ph.D.

Geodesist, National Geodetic Survey, National Oceanic and Atmospheric Administration

1315 East-West Highway, SSMC3 Silver Spring, MD 20910, U.S.A; former Assistant Professor, Civil and Construction Engineering, Oregon State University.

E-mail: daniel.gillins@noaa.gov

[1] Corresponding Author; daily phone: 541 908 5793

Abstract

In recent years, many have mapped the liquefaction potential index (LPI) to describe the liquefaction hazard at regional scale. Several investigators have calibrated the LPI to field observations of liquefaction-induced ground failure after a number of major earthquakes; the significance of LPI values and their correlation with the severity of liquefaction-induced ground failure can vary greatly depending on the calibration. In this study, the LPI was computed at more than 1200 cone penetration test soundings across the Christchurch area, New Zealand, using peak ground accelerations from the 2011 Christchurch Earthquake. Based on detailed field observations of liquefaction-induced ground failure after the earthquake, it was shown that the LPI has potential for discriminating between areas with no liquefaction-induced ground failure hazard and areas that may experience liquefaction-induced ground oscillations and settlement; however, the LPI performed poorly at sites where severe ground failures occurred, especially at sites that experienced lateral spreading . As many researchers have found a positive correlation between the amount of lateral spread and the proximity and depth of a nearby free-face (i.e., a steep topographic depression, river channel, etc.), a new LPI framework was proposed that includes a parameter named the free-face ratio (*FFR*). *FFR* was shown to have a significant correlation with field observations of in Christchurch. It was shown that by incorporating *FFR* into the LPI framework, modified LPI values are positively correlated with the severity of field observations of liquefaction-induced ground failure in Christchurch. It was also shown that maps can be produced based on LPI and *FFR*, and such maps rarely underpredict the liquefaction-induced ground failure hazard, unlike maps based on the unmodified LPI.

Keywords: Liquefaction, Earthquake, LPI, Mapping, Free Face, Lateral spread

1. Introduction

Loosely deposited, cohesionless, and saturated soils may liquefy during cyclic loading, such as from a major earthquake. When the cyclic loads cause excess pore water pressure in these soils to equal and counteract confining stresses, liquefaction will occur. Liquefaction may induce a number of ground failures of varying severity, including: sand boils as the excess pore water pressures become so great that liquefied soil is ejected to the ground surface; ground settlement as loose, cohesionless soils tend to dilate during liquefaction; ground cracks as blocks of mostly intact soil above a liquefied layer collide together and oscillate during ground shaking; lateral spread as mostly intact blocks of soil above a liquefied layer may displace down a gentle slope or towards a free-face (i.e., such as a steep topographic depression or channel); and flow failures, as blocks of soil above a liquefied layer slide violently down steep slopes resulting in catastrophic damage and even loss of life.

Although a variety of different types of ground failures may occur due to liquefaction, a popular method today is to map liquefaction hazard based on a single "intensity parameter" that is meant to describe the severity of *all* potential liquefaction-induced ground deformations. Such liquefaction hazard maps are meant to be easy for users to read and interpret. If the intensity parameter is well-calibrated and effective, then as the mapped intensity parameter increases, then the severity of liquefaction-induced ground failures should increase as well.

Iwasaki et al. (1978) introduced a popular intensity parameter, known as the Liquefaction Potential Index (LPI). Over a dozen researchers in the past 20 years have published microzonation and probabilistic liquefaction hazard mapping methods based on the LPI as an intensity parameter (e.g., Holzer et al., 2006; Sonmez, 2003; Sonmez and Gokceoglu, 2005; Papathanassiou et al., 2005; Baise et al., 2006; Lense and Baise 2007; Yalchin et al., 2008).

Although the LPI is popular, there is evidence that it under-predicts the liquefaction hazard at sites that can undergo liquefaction-induced lateral spreading. For instance, at numerous sites with low LPI values, severe ground failures due to lateral spread occurred in Christchurch, New Zealand, after the 2010-2011 Canterbury Earthquake Sequence (Maurer et al. 2014). The objective of this paper is to propose a modification to the LPI so that LPI-based hazard maps are able to more correctly identify sites prone to lateral spread—one of the most severe types of liquefaction-induced ground failures. To accomplish this objective, an extensive case history database from New Zealand was evaluated as well as field observations of liquefaction after the 2011 Christchurch Earthquake. Using numerous cone penetrometer tests (CPTs), aerial lidar data, and measurements of groundwater depth, hazard maps based on unmodified LPI values were developed and again found to under-predict the liquefaction ground failure hazard at sites where there were field observations of lateral spreading. Afterwards, markedly improved maps were developed based on adding topographic variables to the LPI.

2. Background on the LPI

Iwasaki et al. (1978) defined the LPI according to Eq. 1.

$$LPI = \int_0^{20m} F \cdot w(z) \cdot dz \quad (1)$$

where F (defined in Eq. 2) is a severity term equal to the amount by which the factor of safety (FS) against liquefaction triggering of a layer of soil is less than one, and $w(z)$ is shown in Eq. 3 as a weighting factor that is a function of the depth (z) in meters.

$$F = \begin{cases} 1 - FS & \text{for } FS \leq 1 \\ 0 & \text{for } FS > 1 \end{cases} \quad (2)$$

$$w(z) = 10 - 0.5z \quad (3)$$

As can be seen in Eqs. 1 through 3, the LPI is a function of: the cumulative thickness of the upper 20 meters of soil at a site with a value of FS less than 1; the amount by which FS is less than 1; and, the proximity of the liquefied soils to the ground surface. Because surface effects from liquefaction at depths greater than 20 meters are rarely identified or reported, the integral in Eq. 1 is limited to a depth of 20 meters. *FS* in Eq. 2 is most commonly found by the "simplified procedure" using geotechnical in situ tests, as originally introduced by Seed and Idriss (1971). *FS* is computed by dividing the capacity of the layer of soil to resist liquefaction, expressed in terms of the cyclic resistance ratio (*CRR*), by the seismic demand imposed by the earthquake, expressed in terms of the cyclic stress ratio (*CSR*). If *CSR* exceeds *CRR* for a layer, then $FS < 1$ and liquefaction in that layer is expected.

$$FS = \frac{CRR}{CSR} \quad (4)$$

In the simplified procedure, *CSR* is defined according to Eq. 5.

$$CSR = 0.65\left(\frac{a_{max}}{g}\right)\left(\frac{\sigma_{vo}}{\sigma'_{vo}}\right)MSF \cdot r_d \quad (5)$$

where a_{max} is the earthquake peak ground acceleration (PGA) at the ground surface; g is gravitational acceleration; σ_{vo} and σ'_{vo} are total and effective overburden stresses, respectively; MSF is the magnitude scaling factor; and, r_d is a stress reduction coefficient.

CRR is commonly found by empirical models that relate in-situ geotechnical data (e.g., number of Standard Penetration Test (SPT) blows, CPT tip resistance, etc.) to previous cases of liquefaction. Numerous geotechnical models exist, and excellent summaries of popular models can be found in Youd et al. (2001) and Idriss and Boulanger (2008).

One of the advantages of the LPI model is that it integrates the factors of safety against liquefaction triggering for the upper 20 meters of the soil column into a single, unique value between 0 and 100. These single, unique values are much easier to show on 2D maps than individual factors of safety for each layer of a soil column (Papathanassiou, 2008).

Iwasaki et al. (1982) evaluated the LPI at 85 sites in Japan for six different earthquakes and concluded that surface manifestations of liquefaction is extremely likely at sites with LPI > 15, and low at sites with LPI < 5. Hereinafter, these values are referred to as the "Iwasaki Scale".

More recently, several investigators have evaluated the LPI and the Iwasaki Scale with recent case histories of liquefaction. Due to the uncertainties in the soil profiles and cyclic loads induced by the earthquakes, Sonmez (2003) modified the LPI framework such that the computation of *F* included layers of soil with *FS* as high as 1.2. After calibrating this conservative modification to the LPI framework with case histories of liquefaction, Sonmez then provided a new significance scale for LPI values. Table 1 presents this scale and compares it with the Iwasaki Scale.

Toprak and Holzer (2003) analyzed a database of 243 CPT soundings for 5 historical earthquakes (with magnitude ranging from 6.5 to 6.9) in California (i.e., Imperial Valley 1979, Loma Prieta 1989, San Fernando 1971, Superstition Hills 1987, and Northridge 1994). They computed *FS* with depth at every CPT sounding using an empirical model detailed in Robertson and Wride (1998), and then computed LPI values according to Eqs. 1 through 3. They found that the LPI values were generally higher in liquefied areas than in the non-liquefied areas; but, they concluded that the LPI could not clearly discriminate between sites with surface manifestations of liquefaction, and sites without surface manifestations. When evaluating the severity of the liquefaction-induced ground failures for the California case histories, they concluded that the significance of the LPI values were generally in agreement with the Iwasaki Scale. Based on median LPI values for each ground failure type, they concluded that sand boils were likely when LPI > 5, and that lateral spreading is likely at sites with LPI > 12. Figure 1 is a box-and-whisker plot of their LPI values for each ground failure type. It is important to note the large range of LPI values at the lateral spreading case histories, and that some lateral spreading sites even had LPI values less than 5. The authors hypothesize that this large range may be evidence that the LPI is not well suited for describing lateral spread, and that other influential factors needed to be incorporated in the LPI model to account for this severe ground failure category.

Lee et al. (2004) analyzed 72 CPT soundings after the 1999 Chi-Chi, Taiwan, earthquake (magnitude 7.6). They computed the LPI at each CPT in the same manner as Toprak and Holzer (2003). However, they found that 85% of the non-liquefied cases had values of LPI > 5, and that 30% even had values of LPI > 15. They recommended greatly modifying the Iwasaki Scale, stating that surface manifestations of liquefaction are extremely likely at sites with LPI > 21, and low at sites with LPI < 13.

Some investigators have also developed reliability-based approaches to account for the uncertainties in the LPI computations (e.g., Jha and Suzuki, 2009; Juang et al., 2003; Li et al., 2006; Juang et al., 2008; Sonmez and Gukceoglu, 2005). Jha and Suzuki (2009) investigated the variability of the factors of safety against liquefaction triggering, and concluded that high uncertainties may yield erroneously high values of LPI. They suggested that when generating hazard maps, a reliability-based method should be used; however, they did not develop a probabilistic method for calculating the LPI.

Li et al. (2006) evaluated a database of 155 CPT soundings from several places in the world (US, Turkey and Taiwan), and computed *FS* at every CPT according to the Juang et al. (2006) liquefaction triggering models. They also modified Eq. 2 to be based on a probability of liquefaction (P_L) term.

In another probabilistic study, Juang et al. (2008) calibrated the LPI with CPTU (CPT with piezometer) data. They used 75 CPTU soundings from case histories of the 1999 Chi-Chi, Taiwan, and the 1999 Kocaeli, Turkey, earthquakes. They concluded that the Iwasaki Scale is not universally applicable, and that the significance scale of LPI values should be recalibrated whenever there is a change to the LPI equations or use of a different model for computing *FS*. They also developed a model for estimating the conditional probability of surface manifestations of liquefaction (P_G). Based on risk categories developed in Li et al. (2006), Juang et al. (2008) found that 83% of the non-liquefied sites plotted in low and extremely low risk categories, 17% in the medium category, and none in the high risk category. For liquefied case sites, 82% plotted in high and extremely high risk categories, 16% in medium, and 2% in low risk category.

Papathanassiou (2008) compiled 79 SPT borings from several case histories of earthquakes in Taiwan, Turkey and Greece, and then calculated *FS* according to an SPT-based procedure recommended in Youd et al. (2001). After computing LPI values at each SPT and calibrating them with field observations of liquefaction, Papathanassiou (2008) found that the Iwasaki Scale needed to be significantly modified. Based on the results of the study, three categories were defined for classifying the severity of liquefaction-induced ground failures: (1) no failure when LPI < 19; (2) high when LPI > 32; and (3) medium severity if LPI is in between 19 and 32.

Kang et al. (2014) recalibrated the significance scale of LPI values by investigating a case history database for the 2004 Niigata-Ken Chuetsu, Japan, earthquake. They used 376 SPT logs that were collected from 1996 to 2006. After calculating *FS* and LPI in the same manner as Papathanassiou (2008), they suggested lower threshold values for the 3 liquefaction severity categories: (1) low to no failure when LPI < 14; (2) high when LPI > 21; and (3) moderate severity if LPI is in between 14 and 21.

In one of the latest investigations, Maurer et al. (2014) evaluated a large and comprehensive geotechnical database that included nearly 1200 CPT soundings and detailed field observations of liquefaction after the 2010 Darfield and 2011 Christchurch earthquakes in New Zealand. Similar to Toprak and Holzer (2003), they computed *FS* with depth at each CPT according to the Robertson and Wride (1998) triggering model. They then developed box-and-whisker plots depicting distributions of LPI values according to six liquefaction-induced ground failure severity categories (see Figure 2). Table 2 gives detailed descriptions of each of the six ground failure severity categories. As can be readily seen in Figure 2, the distributions of LPI values generally increase for the first 4 ground failure severity categories. However, the two most severe ground failure categories (some "lateral spreading" and "severe lateral spreading") do not follow this trend. Maurer et al. (2014) concluded that the LPI is not well suited for predicting lateral spreading hazards. This important finding underscores the need to modify the LPI framework. If the LPI cannot be used to map lateral spread hazards, then it is a hardly valuable intensity parameter for describing the potential severity of liquefaction-induced ground failures. An intensity parameter is only valuable if it is positively correlated with ground failure severity. Lateral spread is considered the most pervasive type of liquefaction-induced ground failure (NRC 1985); thus, it is important that the intensity parameter used in liquefaction hazard mapping is capable of identifying this severe ground failure type.

The LPI likely omits important factors that influence the severity of lateral spreading. Numerous investigators have found a positive statistical correlation between the amount of horizontal displacement due to lateral spreading and the degree of ground slope and/or the proximity and height of a nearby free face (e.g., Bartlett and Youd, 1995; Rauch and Martin, 2000; Youd et al., 2002; Zhang et al., 2004; Faris et al., 2006; Gillins and Bartlett, 2013). Due to a lack of confinement and gravity, mostly intact blocks of soil above a liquefied layer tend to spread laterally down gentle slopes or towards free-faces.

It is clear that topography influenced the severity of liquefaction-induced ground failures in the Canterbury region of New Zealand during the 2010-2011 Canterbury Earthquake Sequence (CES). Thus, this paper investigates the addition of a topographic variable to the LPI framework, known as the free-face factor. As will be shown, resulting modified LPI values could then be positively correlated with all six ground failure categories defined in Table 2 (i.e., including the 2 lateral spreading categories).

3. Source of Data and Processing Methodology

Several major earthquakes causing surface manifestations of liquefaction struck the Canterbury region in New Zealand from 2010 through 2011. To help assess damage from these earthquakes, the Earthquake Commission (EQC) and the Canterbury Earthquake Recovery Authority (CERA) have overseen the compilation of an incredibly extensive geotechnical database, named the Canterbury Geotechnical Database (CGD). The CGD can be accessed online at https://canterburygeotechnicaldatabase.projectororbit.com. The CGD also includes ground motion records, measurements of groundwater depths, some SPT logs, and field observations of liquefaction after major earthquakes of the CES. Such an extensive database provides a unique opportunity to investigate liquefaction hazard mapping methods with detailed data at a regional size and scale. Shortly after each major earthquake, field observations of surface manifestations of liquefaction were carefully mapped according to the six detailed categories that are defined in Table 2. Although liquefaction may have occurred at certain depths, only areas with surface manifestations of liquefaction were identified as "liquefied areas."

The Christchurch area and its vicinity in New Zealand were severely affected by the February 2011 Christchurch earthquakes with a magnitude of 6.2. After the earthquake, widespread surface manifestations of liquefaction occurred. Although the magnitude of the Christchurch earthquake was not very high, its seismic source was shallow and close to the Christchurch Metropolitan Area, resulting in high peak ground accelerations in populated and developed areas and great damage to infrastructure.

Figure 3 illustrates the boundaries of the Christchurch area that was included in this study, and it depicts field observations of liquefaction in the Christchurch area due to the 2011 Christchurch earthquake. It also shows the location of thousands of CPT soundings that were downloaded from the CGD.

According to Eq. 1, LPI requires integration over the upper 20 meters of the soil column. However, many CPT soundings met refusal or a hard layer (e.g., where the cone tip resistance was greater than 20 MPa) before reaching a depth of 20 meters. Densely deposited, non-liquefiable, Pleistocene gravels known as the Riccarton Gravel formation underlay loosely deposited and potentially liquefiable alluvial soils known as the Christchurch formation. The Christchurch formation consists of the liquefiable soils that are important to this study. Because of its density and age, the Riccarton Gravel formation is not considered liquefiable, and it is possible to reach this formation at very shallow depths—especially on the west end of the study area. Brown et al. (1995) noted that the thickness of the Christchurch formation is the greatest (i.e., ~40 m) near the present-day coastline, and becomes thinner moving inland. This is in agreement with the termination depth of the CPT soundings in the CGD, as shown in Figure 4. As can be seen, the termination depths of the CPT soundings generally exceed 20 meters near the Pacific Coastline, and termination depths become shallower moving westward.

Only 771 of 1489 soundings exceeded a depth of 20 meters; however, it was assumed in this study that most of the CPT soundings were terminated upon reaching the Riccarton Gravel formation, and that the CPT soundings were pushed through the entire Christchurch formation. To investigate if any CPT soundings were terminated earlier than 20 meters but *not* at refusal due to the Riccarton Gravel formation, the CPT database was first parsed using an "Anselin Local Moran I" analysis (Anselin, 1995). Maurer et al. (2014) used the same analysis procedure when evaluating some of the CPT data from the CGD. This analysis test identifies soundings with termination depths that are statistically less than the spatial average. Based on the results of this test, 254 soundings were removed from further analysis, as they may have terminated before reaching the gravel formation. From the 1235 remaining soundings, 214 had a termination depth of less than 10 meters, 250 had a termination depth between 10 and 20 meters, and 771 soundings had termination depths greater than 20 meters.

To further evaluate our assumptions on CPT termination depths, the database of soundings was divided into two sets: (1) all 1235 of the CPT soundings in the study area; and (2) only CPT soundings with termination depths greater than 20 m.

Factors of safety against liquefaction with depth were computed at each CPT using the triggering model in Robertson and Wride (1998). Other CPT-based procedures are available (e.g., Juang et al. 2006; Idriss and Boulanger 2006), but several of the previous LPI studies made use of the Robertson and Wride (1998) triggering model (e.g., Toprak and Holzer 2003; Lee et al. 2004; Maurer et al. 2014). Therefore, it was decided to use the popular Robertson and Wride (1998) model to allow a direct comparison of the results with these previous LPI studies. However, future research is to investigate modifying the LPI using newer CPT-based procedures for estimating *FS*.

In Robertson and Wride (1998), the first step is to normalize the cone tip resistance to a "clean-sand" equivalent value at atmospheric pressure, $(q_{c1N})_{cs}$. For more details on this normalization, refer to Youd et al. (2001). Afterwards, CRR is found by Eq. 6.

$$If \quad (q_{c1N})_{cs} < 50 \qquad \frac{CRR}{MSF} = 0.833\left[\frac{(q_{c1N})_{cs}}{1000}\right] + 0.05 \tag{6a}$$

$$If \quad 50 \leq (q_{c1N})_{cs} < 160 \qquad \frac{CRR}{MSF} = 93\left[\frac{(q_{c1N})_{cs}}{1000}\right]^3 + 0.08 \tag{6b}$$

The stress reduction coefficient, r_d, is calculated by using models that were developed in Liao and Whitman (1986). The models are shown in Eq. 7.

$$r_d = 1 - 0.00765z \qquad for \qquad z \leq 9.15\ m \tag{7a}$$

$$r_d = 1.174 - 0.0267z \qquad for \qquad 9.15\ m \leq z \leq 23\ m \tag{7b}$$

The magnitude scaling factor (MSF) is calculated according to the Seed and Idriss (1982) model, as shown in Eq. 8.

$$MSF = \frac{10^{2.24}}{M_w^{2.56}} \quad (8)$$

To estimate the total and effective vertical stresses with depth, soil unit weights were estimated from the CPT data using methods in Robertson and Cabal (2010). Depths to the groundwater table (GWT) were taken from the CPT sounding logs, as downloaded from Canterbury Geotechnical Database (CGD, 2013c). The GWT depths reported on these logs were primarily found from pore-pressure dissipation tests (CGD, 2013c). Layers of soil above the GWT were assigned a value of *FS* greater than 1.

Mapped values of a_{max} for the Darfield and Christchurch earthquakes were downloaded from the CGD (CGD 2013d). These maps are based on interpolation of a_{max} values recorded at nearby strong ground motion stations, and from empirical ground motion models of fault rupture proposed by Bradley (2010). Figure 5 shows a raster image of a_{max} for the Christchurch earthquake. By sampling a_{max} values at every CPT from this image, *FS* was afterwards computed at every 1 or 2 cm depth intervals, coincident with the measurement rate of the CPT soundings. Following recommendations in Robertson and Wride (1998), layers with a soil behavior type index, I_c, greater than 2.6 were considered too plastic to liquefy. For these plastic layers of soil, *FS* was assigned to be greater than 1 (i.e., not liquefiable).

After solving for *FS* with depth, the LPI was then computed at all 1235 CPT soundings according to Eqs. 1 through 3. These LPI values are referred to in this paper as "LPI_o" values to differentiate them from the later, modified LPI values developed in this paper.

4. Results and Discussion

4.1. Predicting the Severity of Liquefaction-Induced Ground Failures with the LPI

Iwasaki et al. (1978) originally developed the LPI for predicting the potential severity of surface manifestations of liquefaction. To evaluate the effectiveness of the LPI for predicting the severity of liquefaction-induced ground failures in New Zealand, Figure 6 shows box-and-whisker plots of the computed LPI_o values for: (a) all 1235 CPT soundings in the study; and (b) only CPT soundings with termination depths that exceeded 20 meters. The same general trend is observed for the box-and-whisker plots shown in Figure 6a and 6b; thus, all 1235 CPT soundings were used for the remainder of this study. In general, the median LPI_o values in each category increase for the first four field observation categories; however, the medians do not continue to increase for categories 5 and 6. Note that the trend of the box-and-whisker plots shown in Figure 6 follow the same trend as shown in Figure 3 per Maurer et al. (2014). The median LPI_o values for sites in ground failure categories 1 through 4 are 3.6, 7.1, 10.4 and 15.6, respectively. These results are fairly consistent with the Iwasaki Scale; however, the median values of LPI_o at sites with lateral spreading do not follow the same trend as the first 4 categories. The median LPI_o values for ground failure category 5 (i.e., sites with moderate lateral spreading < 1 m cumulative and large cracks), and 6 (i.e., sites with severe lateral spreading ≥ 1 m cumulative and large open cracks) are 12.4 and 15.8, respectively. As shown in Figure 6, the box-and-whisker plot for category 5 looks similar to category 3, and the box-and-whisker plot for category 6 looks similar to category 4. We conclude that the LPI_o is not able to properly identify sites prone to lateral spreading, the most severe type of liquefaction-induced ground failure identified after the Christchurch earthquake.

In the following section, we investigate adding a topographic factor to the LPI framework, namely, a free-face ratio, in order to improve the correlation between LPI values and the severity of liquefaction-induced ground failures.

4.2. Computing the Free-Face Ratio at Each CPT

Bartlett and Youd (1995) found that the amount of ground displacement due to lateral spread rapidly diminishes with increasing distance from a free-face (e.g., river channel, steep topographic depression). In addition, the height of the free-face was found to be positively correlated with the amount of lateral spread displacement. They combined these two topographic variables into a single factor known as the "free-face ratio". The free-face ratio was defined to equal the ratio of the height of the free-face (*H*) to the distance from the free-face (*L*), expressed in percent (Eq. 13).

$$FFR = \frac{H}{L} \, . 100\% \tag{9}$$

Figure 7 outlines the workflow used for estimating *FFR* at each CPT sounding, as proposed in Gillins (2014). This workflow was accomplished using tools and extensions in ESRI ArcGIS® software.

First, we made use of high-resolution aerial lidar data which was collected on 5 September 2010, overseen by the Ministry of Civil Defense and Emergency Management, New Zealand government (CGD, 2013e). The lidar data from the CGD had already been filtered to represent the bare earth surface, and elevation returns were available approximately every meter along the ground surface. A digital elevation model (DEM) of the study area was then constructed from the lidar data (see Figure 8). To account for occasional small gaps in the lidar point cloud, the data was first resampled using bilinear interpolation so that the resulting DEM images had a cell size of 3 meters by 3 meters. Elevations at all of the CPT soundings were then determined by sampling from the DEM.

To identify the free-faces in the study area, the “hillshade” tool in ArcGIS® was used to shade the DEM; in addition, the “slope” tool was used to find sudden, steep changes in slope (i.e., slope > 10%) where free-faces are likely present. For the Christchurch study area, notable free-faces were readily identified along the Avon River and its tributaries. Using tools in LP360 for ArcGIS®, the lidar returns with the lowest elevations near the identified free-faces were identified and extracted for eventually determining *FFR* at every CPT. Unfortunately, the available lidar data did not penetrate into the water; therefore, only the elevation of the top of the water along each side of the Avon River could be determined. In an effort to further refine the estimate of the height of the channel for the Avon River, the depth of the river was first calculated at four monitoring points provided by the Christchurch City Council (CCC). Similar to a study completed by Van Ballegooy et al. (2014), the depth of the river was assumed and simplified to increase linearly between the reported median depths at these four monitoring stations. Then, the elevation of the bottom of the sides of the river channel were estimated and mapped by subtracting the elevation of the top of the water (from the lidar point returns) with the interpolated depth of the river. A better approach would have been to use the results of a hydrographic survey of the elevation and profile of the river channel; however, this type of data were not available for this study.

Free-face ratios were computed from each CPT to every point along the bottom of a channel or steep topographic depression. Then, assuming the lateral displacement will travel towards the largest free-face, or on the path of “least resistance,” the largest computed free-face ratio was assigned as *FFR* for each CPT.

Figure 9 shows box and whisker plots of *FFR* according to field observations of liquefaction-induced ground failure at all CPT soundings. As can be seen, *FFR* is generally less than or around 1-2% for the first 4 ground failure categories where lateral spreading did not occurred. However, for sites in categories 5 and 6 where lateral spread occurred, large *FFR* values occur with medians of 8 and 13, respectively. Figure 10 depicts empirical cumulative distribution function (CDF) of *FFR* for each of the six categories. The figure shows that nearly 70% of the CPT soundings in categories 1 to 4 had a value of *FFR* less than 1%; and, nearly 80% of the CPT soundings in these categories have a *FFR* value less than 3%. All of these CDFs are stacked upon each other, evidence that *FFR* has no influence on these types of ground failures. However, the CDFs of categories 5 and 6 do look distinctively different; Figure 10 shows that the amount of lateral spread is correlated with *FFR*. Over 80% of the CPT soundings in category 5 had a value of *FFR* > 1%; and, all of the CPT soundings in category 6 (severe lateral spreading) had a value of *FFR* > 1%.

With the DEM, it was also possible to calculate slopes at each of the CPT soundings and investigate if the degree of ground slope influenced lateral spreading. Such an analysis was done similar to what was explained above for *FFR*. We found that the slopes in the study area were mostly small (i.e., < 1%, except, of course, at the face of a free-face), and we could not find a correlation between slope and lateral spreading. As mentioned previously, slopes have been found to influence the amount of lateral spread displacement (e.g., Bartlett and Youd 1995; Youd et al. 2002; Gillins and Bartlett 2013). However, for this project, the study area was simply too flat to investigate how the ground slope influenced lateral spreading. Researchers mapping liquefaction hazards in other areas with sloping terrain are cautioned to consider ground slope as an important contributor to the severity of lateral spreading.

4.3. Modifying the LPI framework to include FFR

FFR appears to be a strong contributor to the amount of lateral spreading, and we next investigated methods for modifying the LPI framework to include a variable for *FFR*. Multinomial logistic regression is one statistical method for deriving an empirical model based on more than two categorical dependent variables. For this case, there are six ground-failure categories and two independent variables, *FFR* and LPI. This type of regression would provide the probability that a site is in each of the six categories for an estimated value of *FFR* and LPI. Although this is an attractive method rooted in statistics, it would yield six equations and six maps depicting the probabilities for each category. Such an approach deviates from some of the simplicity and practicality of how the LPI framework was originally developed by Iwasaki et al. (1978), and it also does not fulfill the objective of developing a single parameter for producing a single map depicting the potential severity of the liquefaction-induced ground failure hazard.

Accordingly, a simpler approach was taken to include *FFR*. Previous research has found that free-face ratios are logarithmically correlated with the magnitude of lateral spread displacement (e.g., Bartlett and Youd 1995; Youd et al. 2002; Zhang et al. 2004; Gillins and Bartlett 2014). Thus, the following model is proposed:

$$LPI^{*} = LPI_0 + b \cdot ln(FFR) \qquad \text{where } FFR \geq 1\% \qquad (10)$$

Where LPI^{*} is the modified value of LPI that is a function of *FFR* (in percent) at a site, and LPI_o is the original value of LPI computed at each site according to Eqs. 1 to 3. If *FFR* is computed to be less than 1%, then it must be set to equal 1% for entry in Eqn. 10.

An advantage of using the natural logarithm of *FFR* is that for categories 1 through 4, *FFR* was typically less than or equal to 1%. Setting *FFR* to equal 1%, the right term in Eq. 10 cancels and *FFR* would not be influential for these four ground-failure categories.

Eqn. 10 cannot be linearly regressed, because the independent variable, LPI^*, is not known. However, by the definitions given, it is reasonable to assume that $LPI^* \approx LPI_o$ for ground-failure categories 1 through 4. The median LPI_o values in Figure 6a for these first four categories follow a linear trend. In increments of 0.1, we iterated values of b, computed LPI^* at each of the 1235 CPT soundings, and then computed median LPI^* values for the CPTs within each of the six mapped ground-failure categories. When $b = 3.0$, the same linear trend continues for all six ground failure categories as was found for the first four categories using only LPI_o. Thus, b was set to 3.0 for all computations of LPI^* in this paper.

Figure 11 depicts box-and-whisker plots of LPI^* according to the six liquefaction-induced ground failure observation categories. The box-and-whisker plots increase with increasing ground failure severity. Figure 12 shows empirical CDF plots for LPI^* according to the six ground failure categories. As can be seen, all six empirical CDFs are distinctively different, except for a small overlap between categories 4 and 5 at LPI^* values between 25 and 30. Nearly 60% of the non-liquefied CPT sites have values of $LPI^* < 6$, while less than 2% have values of $LPI^* > 13$. For the severe lateral spreading sites, only about 6% of the CPT sites have values of $LPI^* < 15$, while over 50% have values of $LPI^* > 22$.

4.4. Spatial Analysis of the Performance of LPI in Christchurch area*

The final goal in this project was to evaluate the spatial performance of mapping the potential severity of liquefaction-induced ground failure using unmodified LPI values (LPI_o) and modified

LPI values (LPI^*). First, LPI_o values were mapped as shown in Figure 13; afterwards, LPI^* values were mapped following the same method, as shown in Figure 14. These maps were created by bilinear interpolation of computed LPI_o or LPI^* values at all of the 1235 CPT soundings in the study, and then the interpolated values were averaged within each cadastral property using the "zonal statistics" Esri ArcGIS toolbox to make them comparable to the map of field observations of liquefaction (Figure 3).

In an attempt to quantify the accuracy of the "predictions" in both maps, a prediction error (E) was computed in a manner similar to what was done in Maurer et al. (2014). First, an expected range for LPI was assigned for each of the ground failure severity categories. Like was done in Maurer et al. (2014), this expected range is somewhat subjective because the LPI distributions, such as the ones depicted as box-and-whisker plots in Figure 11 for LPI^*, have some overlap and are not distinctive. Nevertheless, the expected ranges were assigned based on: (1) assuming that the range of LPI values (whether for LPI_o or LPI^*) should increase with increasing severity of ground failure damage (otherwise, LPI would not be a useful indicator for severity); and (2) that the median values for each box-and-whisker plot from ground failure categories 1 through 4 in Figure 6 and for all six categories in Figure 11 are contained near the middle of each expected range. Accordingly, Table 3 presents the assigned ranges of expected LPI values for each of the six categories.

Using the field observations of liquefaction (per Figure 3), values of E were computed at each cadastral property according to the equations shown in Table 4, which are based on the expected ranges of LPI values from Table 3. For example, at a property where severe liquefaction (i.e., ground failure category 4) was observed after the earthquake, LPI should be expected to be between 14 and 18 per Table 3. If the predicted LPI_o or LPI^* values for this property from Figures

13 or 14 exceeded 18, then $E = LPI^*$ or $LPI_o - 18$. If LPI_o or LPI^* was less than 14, then $E = LPI^*$ or $LPI_o - 14$.

Following the equations in Table 4, Figure 15 depicts values of E for the LPI_o map, and Figure 16 shows values of E for the LPI^* map. Positive values of E indicate overpredictions of the liquefaction-induced ground failure severity hazard, and negative values of E indicate underpredictions. To make the error maps easier to read, values of E are colored according to error categories defined in Table 5.

The error maps based on LPI_o in Figure 15 generally show "accurate predictions" where lateral spreading did not occur. However, large portions of the maps show slight to moderate underpredictions of the liquefaction hazard, and some portions of the maps even show moderate to severe underpredictions. This is expected, because based on Figure 6, the LPI_o often produces overly-small relative indicator values for sites prone to lateral spreading. Error maps based on LPI^* in Figure 16 generally show "accurate predictions" at sites where lateral spreading did not occur as well as at sites where lateral spreads were recorded. Figure 16 shows that the LPI^* has great utility as a single "intensity parameter" for mapping the potential severity of liquefaction-induced ground failure. A few small areas in Figure 16 show over- and under-predictions, which may be due to local, site-specific effects that were neglected as part of this simplified mapping method.

Table 6 compares values of E for LPI_o and LPI^* in terms of the total percentage of the study area within each prediction category. It can be concluded from the table that the majority of inaccurate predictions for LPI_o are due to underpredictions, particularly at sites that underwent lateral spreading. The LPI^* map rarely underpredicted the ground failure hazard; moreover, it also rarely overpredicted the hazard.

Conclusions

An investigation has been carried out to evaluate the influence of topography, such as the proximity and height of a free-face, to the observed severity of liquefaction-induced ground failures after the 2011 Christchurch Earthquake in New Zealand. To accomplish this purpose, more than 1200 CPT soundings in New Zealand were downloaded from the CGD and analyzed. First, LPI values, as originally proposed by Iwasaki et al. (1978), were computed at each CPT sounding. Unfortunately, the LPI does not include any topographic factors; however, it is commonly used as an intensity parameter in modern liquefaction hazard mapping methods. The LPI was found to be effective for predicting the severity of some of the liquefaction-induced ground failures in the study area, such as sand ejecta, failures due to ground oscillations, and vertical deformations. However, the LPI was found to be a poor predictor of lateral spreading, the most severe type of liquefaction-induced ground failure in the study area. Unfortunately, the LPI underpredicts the ground failure hazard at sites that underwent lateral spreading in Christchurch.

As soils generally displace towards free-faces, and since numerous lateral spreads were observed in the study area near river channels, a new parameter was introduced to the LPI model named the free-face ratio (*FFR*). It was then shown that a considerable correlation exists between FFR and the severity of lateral spreading. By modifying LPI to also be a function of *FFR*, a new index was produced named *LPI**. *LPI** was developed to be positively correlated with the increasing severity of liquefaction-induced ground failures in the study area, and it was shown to be a much better predictor of lateral spreading than unmodified LPI (LPI_o). *LPI** was shown to rarely underpredict or overpredict the liquefaction-induced ground failure severity.

Future investigations are necessary to strengthen the analysis and development of *LPI**. Other case studies of earthquakes in different locations should be investigated. In addition, it is well known that other factors contribute to the severity of liquefaction-induced ground failures, such as ground slope. For this study area, we could not find a correlation between percent ground slope and the severity of ground failure. However, this study area was generally flat and the liquefaction-induced ground failures were influenced more heavily by nearby free faces. Additional research could also involve calibrating LPI* using other in situ empirical models for estimating the factor of safety against liquefaction.

References

Anselin, L. (1995). "Local indicators of spatial association—LISA." *Geogr. Anal.*, 27(2), 93–115.

Baise, L. G., Higgins, R. B., and Brankman, C. M. (2006). "Liquefaction hazard mapping—Statistical and spatial characterization of susceptible units." *J. Geotech. Geoenviron. Eng.*, 132:6(705), 705–715.

Bartlett, S. F., & Youd, T. L. (1995). "Empirical prediction of liquefaction-induced lateral spread". *Journal of Geotechnical Engineering*, *121*(4), 316-329.

Bradley, B. A. (2010). “NZ-specific pseudo-spectral acceleration ground motion prediction equations based on foreign models”. *Dept. of Civil and Natural Resources Engineering*, Univ. of Canterbury, Christchurch, New Zealand.

Brown, L. J., et al. "Geology of Christchurch, New Zealand." *Environmental & Engineering Geoscience* 1.4 (1995): 427-488.

Canterbury Geotechnical Database (2013a). "Liquefaction and Lateral Spreading Observations", *Map Layer CGD0300 - 11 Feb 2013*, retrieved from https://canterburygeotechnicaldatabase.projectorbit.com/

Canterbury Geotechnical Database (2013b). "CPT Layer Analysis and Depth of Refusal", *Map Layer CGD0055*, retrieved from https://canterburygeotechnicaldatabase.projectorbit.com/

Canterbury Geotechnical Database (2013c) "Liquefaction evaluation of CPT investigations", *Map Layer CGD0050*, retrieved from https://canterburygeotechnicaldatabase.projectorbit.com/

Canterbury Geotechnical Database (2013d) "Conditional PGA for Liquefaction Assessment", Map Layer CGD5110 - 11 Feb 2013, https://canterburygeotechnicaldatabase.projectorbit.com/

Canterbury Geotechnical Database (2013e). LiDAR and digital elevation models. *Map layer CGD0500* 2013. Retrieved 25 Sep 2013 from https://canterburygeotechnicaldatabase.projectororbit.com/

Faris, A. T., Seed, R. B., Kayen, R. E., & Wu, J. (2006). “A semi-empirical model for the estimation of maximum horizontal displacement due to liquefaction-induced lateral spreading.” In *Proc. 8th US Conference on Earthquake Engineering*, Vol. 3, pp. 1584-1593

Gillins, D. T., & Bartlett, S. F. (2013). “Multilinear Regression Equations for Predicting Lateral Spread Displacement from Soil Type and Cone Penetration Test Data”. *Journal of Geotechnical and Geoenvironmental Engineering*, 140(4), 04013047.

Gillins, D.T. (2014). “Considering topography when mapping liquefaction hazard with the liquefaction potential index.” *Proc. 10th National Conference in Earthquake Engrg. (10NCEE)*, *Earthquake Engineering Research Institute,* Anchorage, AK, 12 pp.

Holzer, T.L., Bennett, M.J., Noce, T.E., Padovani, A.C., Tinsley III, J.C., (2006). “Liquefaction hazard mapping with LPI in the Greater Oakland, California, Area”. *Earthquake Spectra,* 22 (3), 693–708.

Idriss, I. M., & Boulanger, R. W. (2006). “Semi-empirical procedures for evaluating liquefaction potential during earthquakes”. *Soil Dynamics and Earthquake Engineering*, *26*(2), 115-130.

Idriss, I. M., & Boulanger, R. W. (2008). “Soil liquefaction during earthquakes”. *Earthquake Engineering Research Institute*, Oakland, CA.

Iwasaki, T., Arakawa, T., and Tokida, K. (1982). “Simplified procedures for assessing soil liquefaction during earthquakes.” *Proceedings of the Conference on Soil Dynamics and Earthquake Engineering*, Southampton, UK, 925−939.

Iwasaki, T., Tatsuoka, F., Tokida, K., and Yasuda, S. (1978). “A practical method for assessing soil liquefaction potential based on case studies at various sites in Japan.” *Proc., 2nd Int. Conf. on Microzonation, National Science Foundation*, Washington, DC.

Jha, S. K., and Suzuki, K. (2009). “Liquefaction potential index considering parameter uncertainties.” *Eng. Geol*., 107(1–2), 55–60.

Juang, C. H., Yuan, H., Lee, D.-H., and Lin, P.-S. (2003). “Simplified cone penetration test-based method for evaluating liquefaction resistance of soils.” *J. Geotech. Geoenviron. Eng.*,:1(66), 66–80.

Juang, C. H., Yuan, H., Li, D. K., Yang, S. H., & Christopher, R. A. (2006). Estimating severity of liquefaction-induced damage near foundation. *Soil Dynamics and Earthquake Engineering*, 25(5), 403-411.

Juang, C.H., Liu, C.-N., Chen, C.-H., Hwang, J.-H., Lu, C.-C., (2008). “Calibration of liquefaction pontential index: a re-visit focusing on a new CPTU model”. *Eng. Geol.* 102, 19–30.

Kang, G. C., Chung, J. W., & Rogers, J. D. (2014). Re-calibrating the thresholds for the classification of liquefaction potential index based on the 2004 Niigata-ken Chuetsu earthquake. *Engineering Geology*, *169*, 30-40.

Lee, D.-H., Ku, C.-S., and Yuan, H. (2004). "A study of liquefaction risk potential at Yuanlin, Taiwan." *Eng. Geol*., 71(1–2), 97–117.

Lenz, A. J., and Baise, L. G. (2007). "Spatial variability of liquefaction potential in regional mapping using CPT and SPT data." *Soil. Dyn. Earthquake Eng*., 27(7), 690–702.

Li, D.K., Juang, C.H., Andrus, R.D., (2006). "Liquefaction potential index: a critical assessment." *Journal of Geo-Engineering*, Taiwanese Geotechnical Society 1 (1), 11–24.

Liao, S., and Whitman, R. V. (1986). ''Overburden correction factors for SPT in sand.'' *J. Geotech. Engrg.*, 112(3), 373–377.

Maurer, B. W., Green, R. A., Cubrinovski, M., & Bradley, B. A. (2014). Evaluation of the Liquefaction Potential Index for Assessing Liquefaction Hazard in Christchurch, New Zealand. *Journal of Geotechnical and Geoenvironmental Engineering*, 140(7).

National Research Council (NRC). (1985). "Liquefaction of soils during earthquakes," *National Academy Press*, Washington, D.C.

Papathanassiou, G. (2008). “LPI-based approach for calibrating the severity of liquefaction-induced failures and for assessing the probability of liquefaction surface evidence.” *Eng. Geol.*, 96(1–2), 94–104.

Papathanassiou, G., Pavlides, S., and Ganas, A. (2005). “The 2003 Lefkada earthquake: Field observation and preliminary microzonation map based on liquefaction potential index for the town of Lefkada.” *Eng. Geol.*, 82(1), 12–31.

Rauch, A. F., & Martin III, J. R. (2000). “EPOLLS model for predicting average displacements on lateral spreads.” *Journal of Geotechnical and Geoenvironmental Engineering*, 126(4), 360-371.

Robertson, P. K., and Cabal, K. L. (2010). “Estimating soil unit weight from CPT.” *Proc., 2nd Int. Symp. on Cone Penetration Testing,* Int. Society for Soil Mechanics and Geotechnical Engineering (ISSMGE), London, Paper No. 2-40.

Robertson, P. K., and Wride, C. E. (1998). “Evaluating cyclic liquefaction potential using cone penetration test.” *Can. Geotech. J.*, 35(3), 442–459.

Seed, H. B., and Idriss, I. M. (1971). ‘‘Simplified procedure for evaluating soil liquefaction potential.’’ *J. Geotech. Engrg. Div.*, ASCE, 97(9), 1249–1273.

Seed, H. B., and Idriss, I. M. (1982). ‘‘Ground motions and soil liquefaction during earthquakes.’’ *Earthquake Engineering Research Institute Monograph*, Oakland, Calif.

Sonmez, B., Ulusay, R., Sonmez, H., (2008). A study on the identification of liquefaction-induced failures on ground surface based on the data from the 1999 Kocaeli and Chi-Chi earthquakes. *Eng. Geol*. 97 (3–4), 112–125.

Sonmez, H. (2003). “Modification of the liquefaction potential index and liquefaction severity mapping for a liquefaction-prone area (Inegol, Turkey).” *Eng. Geol*., 44(7), 862–871.

Sonmez, H., and Gokceoglu, C. (2005). “A liquefaction severity index suggested for engineering practice.” *Environ. Geol*., 48(1), 81–91.

Toprak, S., and Holzer, T. L. (2003). “Liquefaction potential index: Field assessment.” *J. Geotech. Geoenviron. Eng*.,4(315), 315–322.

Van Ballegooy, S., et al (2014). "Median water table elevation in Christchurch and surrounding area after the 4 September 2010 Darfield Earthquake: Version 2."*GNS Science Report* 18.

Yalcin, A., Gokceoglu, C., and Sönmez, H. (2008). “Liquefaction severity map for Aksaray city center (Central Anatolia, Turkey).” *Nat. Hazards Earth Syst. Sci*., 8(4), 641–649.

Youd, T. L., and Iddriss, I. M. (2001). “Liquefaction resistance of soils: Summary report from the 1996 NCEER and 1998 NCEER/NSF Workshops on Evaluation of Liquefaction Resistance of Soils.” *J. Geotech. Geoenviron. Eng*., 4(297), 297–313.

Youd, T. L., Hansen, C. M., and Bartlett, S. (2002). “Revised multi-linear regression equations for prediction of lateral spread displacement.” *J. Geotech. Geoenviron. Eng*., 12(1007), 1007–1017.

Zhang, G., Robertson, P. K., & Brachman, R. W. I. (2004). “Estimating liquefaction-induced lateral displacements using the standard penetration test or cone penetration test.” *Journal of Geotechnical and Geoenvironmental Engineering*, *130*(8), 861-871.

Table 1. Significance scale of LPI values as proposed by Iwasaki et al. (1982) and Sonmez (2003)

Iwasaki et al. (1982)		Sonmez (2003)	
LPI Value	Liquefaction Severity	LPI Value	Liquefaction Severity
0	Very low	0	Non-Liquefiable
0<LPI<5	Low	0<LPI<2	Low
5<LPI<15	High	2<LPI<5	Moderate
LPI>15	Very High	5<LPI<15	High
		LPI>15	Very High

Table 2. Ground failure severity categories assigned by field observations of liquefaction

Category	Description
1	No observed ground cracking or ejected liquefied material.
2	Some shaking-induced ground surface damage limited to minor cracking and buckling and/or minor undulations. No signs of ejected liquefied material.
3	Generally < 25% of site covered with ejected liquefied material, and/or small cracks (< 50 mm) from ground oscillations. Little to no vertical displacements across cracks and no apparent lateral movement.
4	Generally > 25% of site covered with ejected liquefied material, and/or severe observed ground surface subsidence. Small cracks (< 50 mm) may be present, but little to no vertical displacements across cracks; limited lateral movement.
5	Moderate to major lateral spreading (< 1 m cumulative), and/or large cracks (between 50 to 200 mm) extending across the ground surface with horizontal and/or vertical displacement. Ejected liquefied material often observed.
6	Severe lateral spreading (≥ 1 m cumulative), and/or large open cracks extending through the ground surface with very severe horizontal and/or vertical displacements (≥ 200 mm). Ejected liquefied material often observed.

Table 3. Expected LPI values (either for LPIo or LPI*) for assessing prediction accuracy

Ground Failure Severity Category	Expected LPI range
1. "No Liquefaction"	0-6
2. "Marginal liquefaction"	6-10
3. "Moderate liquefaction"	10-14
4. "Severe liquefaction"	14-18
5. "Lateral spreading"	18-22
6. "Severe lateral spreading"	>22

Table 4. Equations for computing errors (E) for LPI values according to ground failure category

Severity category	Under-prediction And Associated error	Over-prediction And Associated error *
No Liquefaction	—	If LPI or LPI* > 6 E =LPI or LPI* - 6
Marginal liquefaction	If LPI or LPI* < 6 E = LPI or LPI* - 6	If LPI or LPI* > 10 E = LPI or LPI* - 10
Moderate liquefaction	If LPI or LPI* < 10 E = LPI or LPI* - 10	If LPI or LPI* > 14 E = LPI or LPI* - 14
Severe liquefaction	If LPI or LPI* < 14 E = LPI or LPI* - 14	If LPI or LPI* > 18 E = LPI or LPI* - 18
Lateral spreading	If LPI or LPI* < 18 E = LPI or LPI* - 18	If LPI or LPI* > 22 E = LPI or LPI* - 22
Severe lateral spreading	If LPI or LPI* < 22	—

	E = LPI or LPI* - 22	

***Positive and negative errors are associated with over-prediction and under-prediction, respectively.**

Table 5. LPI error classification

Error classification	Error (in units of LPI_o or LPI*)
Moderate to severe under-prediction	$E < -5$
Slight under-prediction	$-5 < E < -2$
Accurate prediction	$-2 < E < 2$
Slight over-prediction	$2 < E < 5$
Moderate to severe over-prediction	$5 < E$

Table 6. Spatial accuracy of LPI_o and LPI^* in terms of total area within each ground failure category.

Error Classification	LPI^* (percent of area within category)	LPI_o (percent of area within category)
Moderate to severe under-prediction	< 1	11.3
Slight under-prediction	3.3	18.9
Accurate prediction	82.5	68.5
Slight over-prediction	12.3	1.1
Moderate to severe over-prediction	1.6	< 1

Figure Caption

Figure 1. Box-and-whisker plots of LPI values versus field observations of liquefaction (after Toprak and Holzer, 2003; with permission from ASCE)

Figure 2. Box-and-whisker plots of LPI values and field observations of liquefaction after the Christchurch and Darfield earthquakes for: (a) all CPT soundings, and (b) CPT soundings with termination depths greater than 20 meters (after Maurer et al. 2014; with permission from ASCE)

Figure 3. Study area near Christchurch, New Zealand, with field observations of liquefaction after the 2011 Christchurch Earthquake and the location of CPT soundings in the CGD.

Figure 4. CPT termination depths in study area

Figure 5. Raster image of peak ground accelerations (a_{max}) in Christchurch area after 2011 Christchurch Earthquake

Figure 6. Box-and-whisker plots of LPI_o values and field observations of liquefaction after the Christchurch Earthquake for: (a) all CPT soundings, and (b) CPT soundings with termination depths greater than 20 meters

Figure 7. Flowchart for calculating *FFR* (the texts in *italic* style are Arc GIS tools or extension)

Figure 8. Digital elevation model (DEM) of study area

Figure 9. Box-and-whisker plots of *FFR* and field observations of liquefaction after the Christchurch earthquake for all CPT soundings

Figure 10. Cumulative distribution functions (CDFs) of *FFR* for all CPT soundings

Figure 11. Box-and-whisker plots of $LPI*$ and field observations of liquefaction after the Christchurch earthquake for all CPT soundings

Figure 12. Cumulative distribution functions (CDFs) of $LPI*$ for all CPT soundings according to field observations of liquefaction. Categories 1 through 6 are defined in Table 2.

Figure 13. Mapped LPI_o values for study area after the 2011 Christchurch Earthquake

Figure 14. Mapped $LPI*$ values for study area after the 2011 Christchurch Earthquake

Figure 15. Error predicted in LPI_o (in LPI_o units) for study area after the 2011 Christchurch Earthquake

Figure 16. Error predicted in $LPI*$ (in $LPI*$ units) for study area after the 2011 Christchurch Earthquake

Figure 1

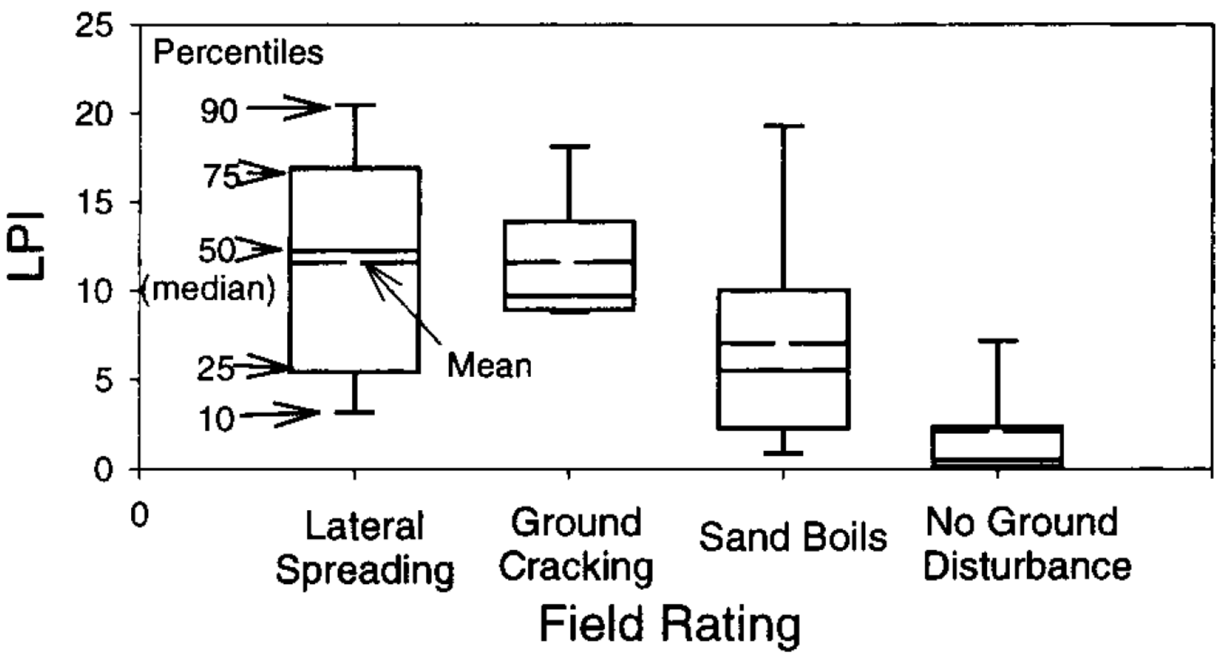
LPI
25
20
15
10
5
0
Percentiles
90
75
50
(median)
25
10
Mean
0
Lateral Spreading
Ground Cracking
Sand Boils
No Ground Disturbance
Field Rating

Figure 2a

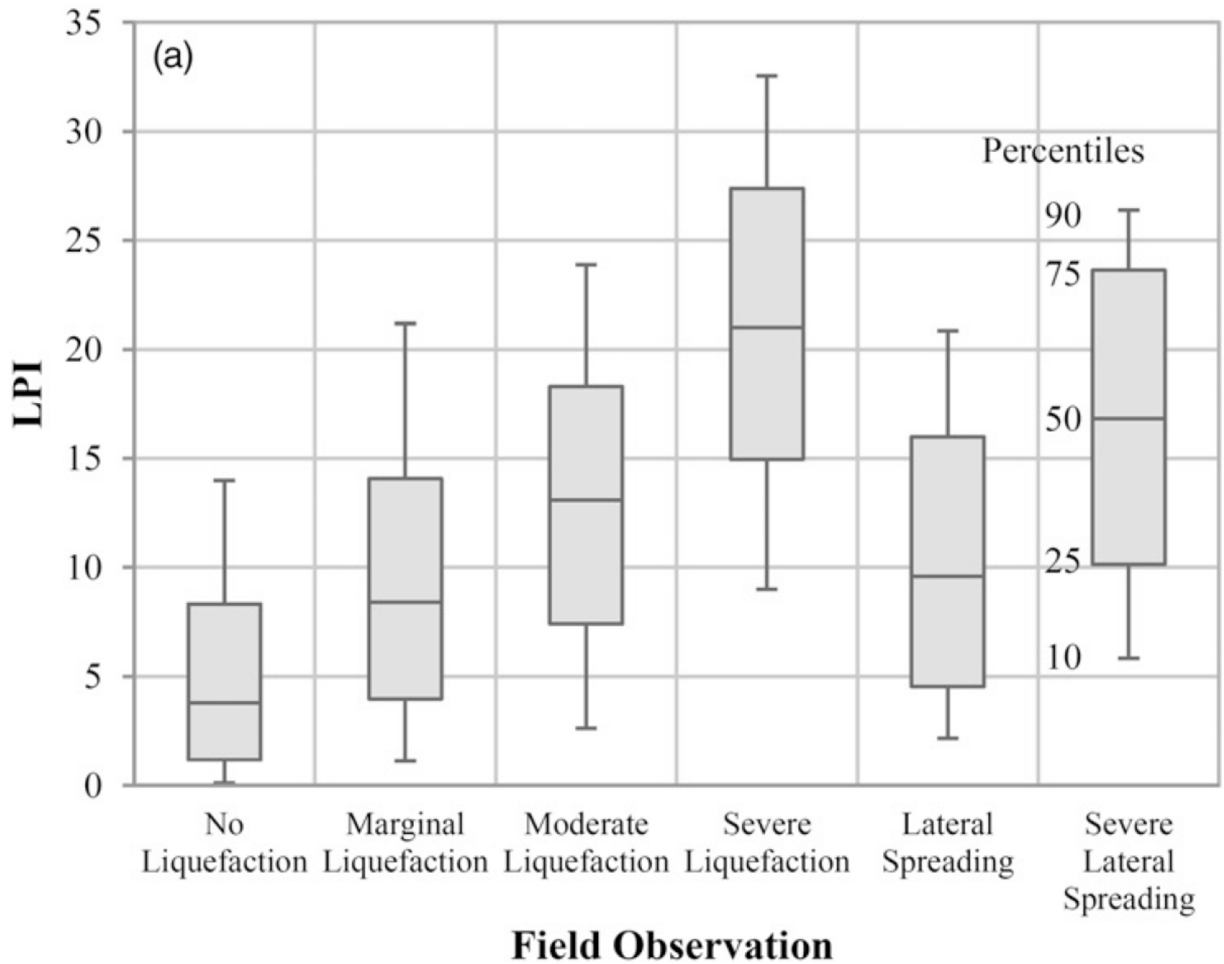
(a)
LPI
35
30
25
20
15
10
5
0
Percentiles
90
75
50
25
10
No Liquefaction
Marginal Liquefaction
Moderate Liquefaction
Severe Liquefaction
Lateral Spreading
Severe Lateral Spreading
Field Observation

Figure 2b

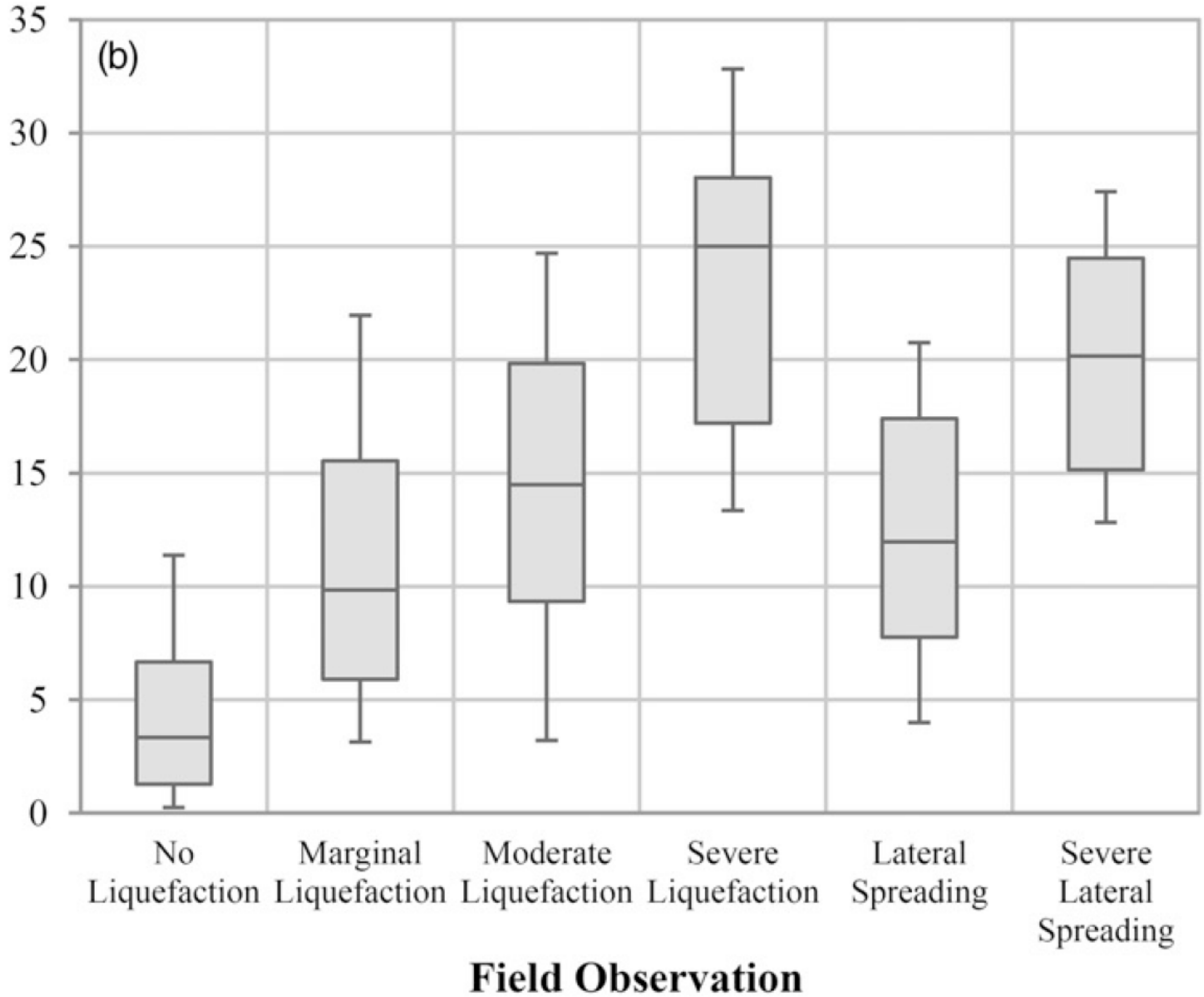
(b)
35
30
25
20
15
10
5
0
No Liquefaction
Marginal Liquefaction
Moderate Liquefaction
Severe Liquefaction
Lateral Spreading
Severe Lateral Spreading
Field Observation

Figure 3

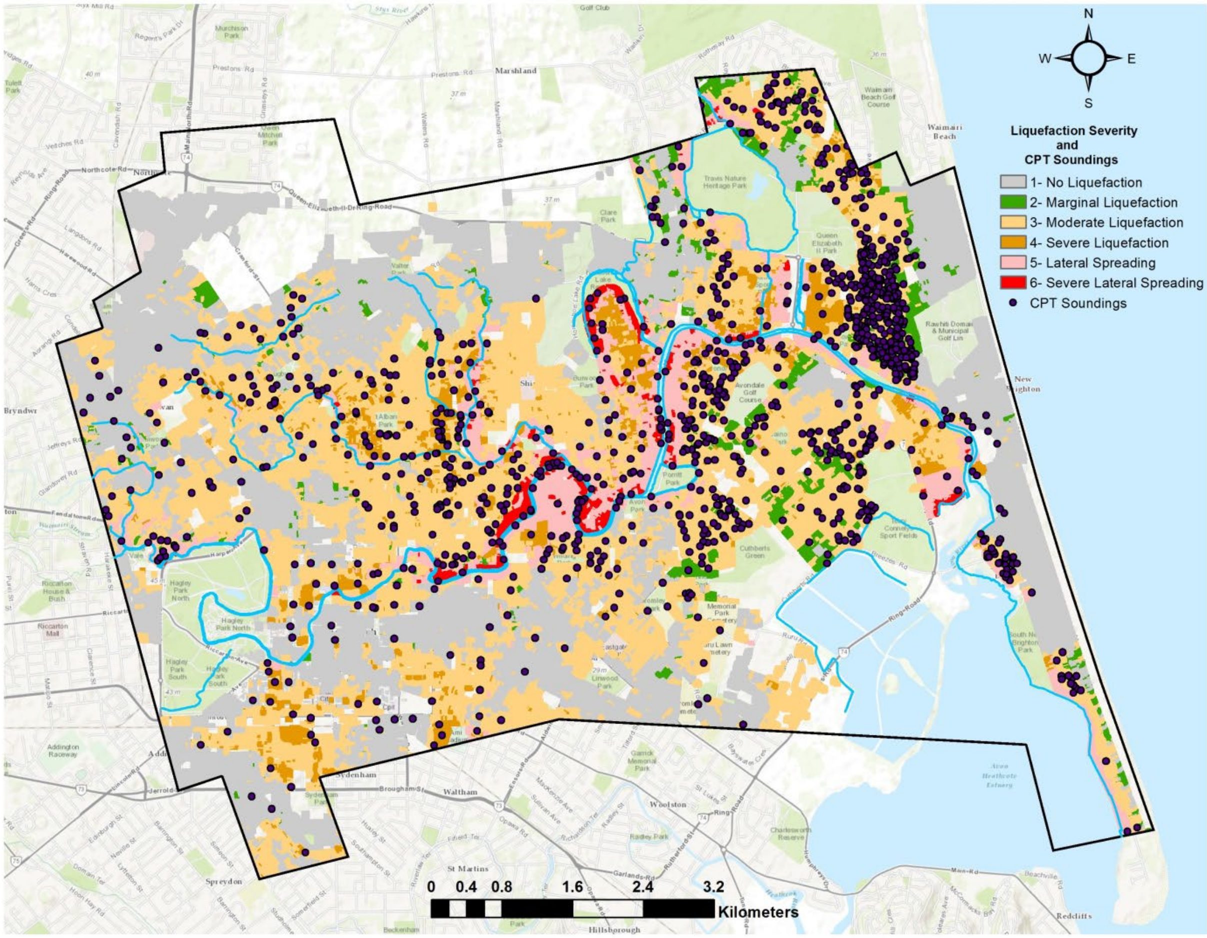
N
W
E
S
Liquefaction Severity
and
CPT Soundings
1- No Liquefaction
2- Marginal Liquefaction
3- Moderate Liquefaction
4- Severe Liquefaction
5- Lateral Spreading
6- Severe Lateral Spreading
CPT Soundings
0 0.4 0.8 1.6 2.4 3.2
Kilometers

Figure 4

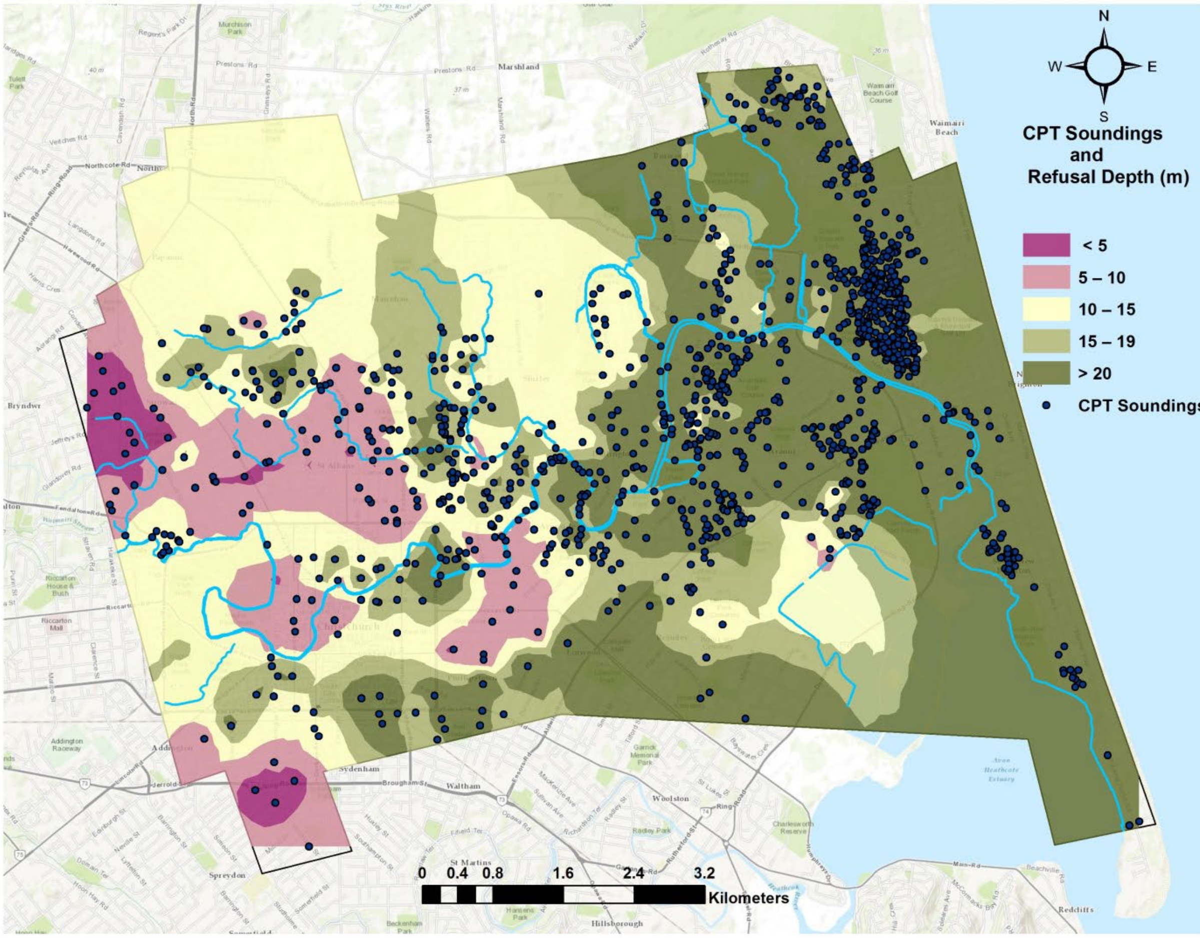
N
W
E
S
CPT Soundings
and
Refusal Depth (m)
< 5
5 – 10
10 – 15
15 – 19
> 20
CPT Soundings
0 0.4 0.8 1.6 2.4 3.2
Kilometers

Figure 5

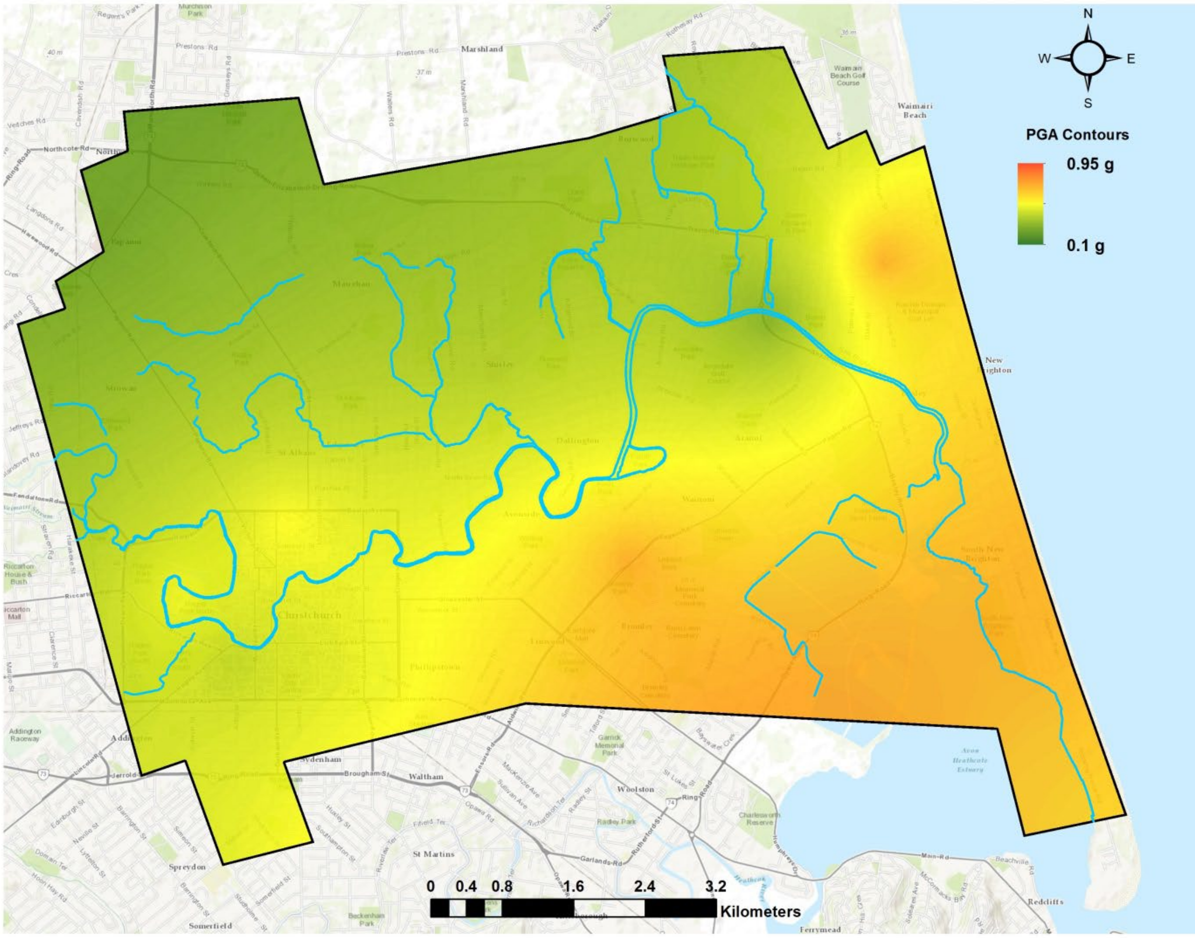

Figure 6a

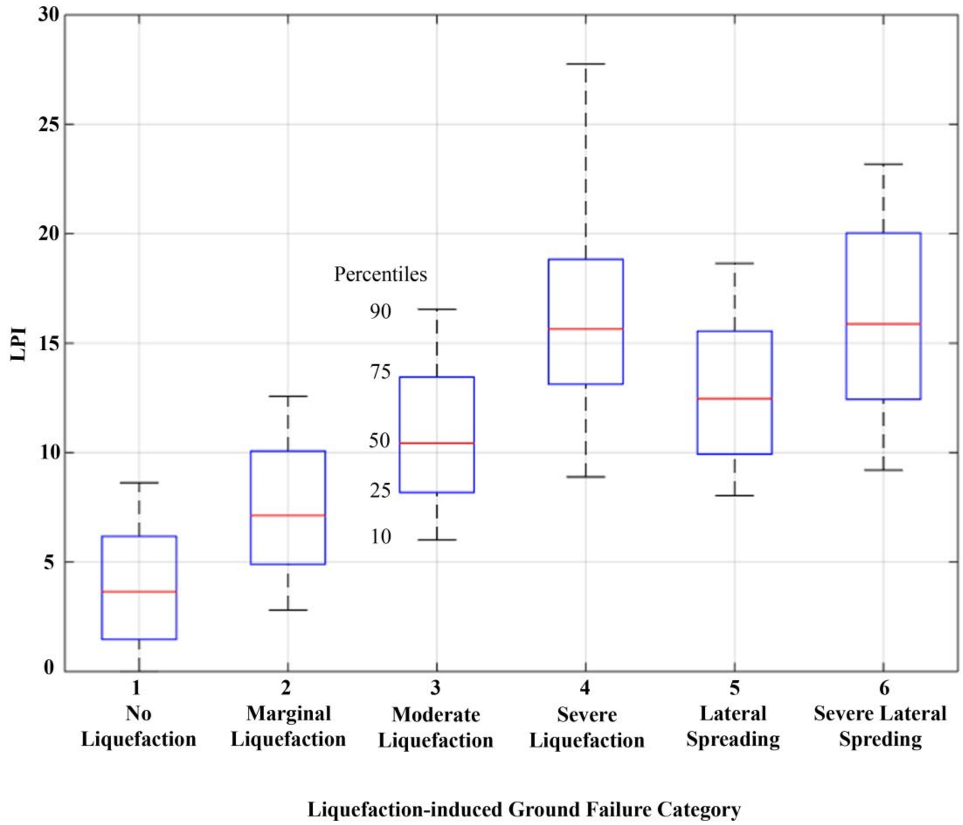
LPI
0
5
10
15
20
25
30
Percentiles
90
75
50
25
10
1
No
Liquefaction
2
Marginal
Liquefaction
3
Moderate
Liquefaction
4
Severe
Liquefaction
5
Lateral
Spreading
6
Severe Lateral
Spreding
Liquefaction-induced Ground Failure Category

Figure 6b

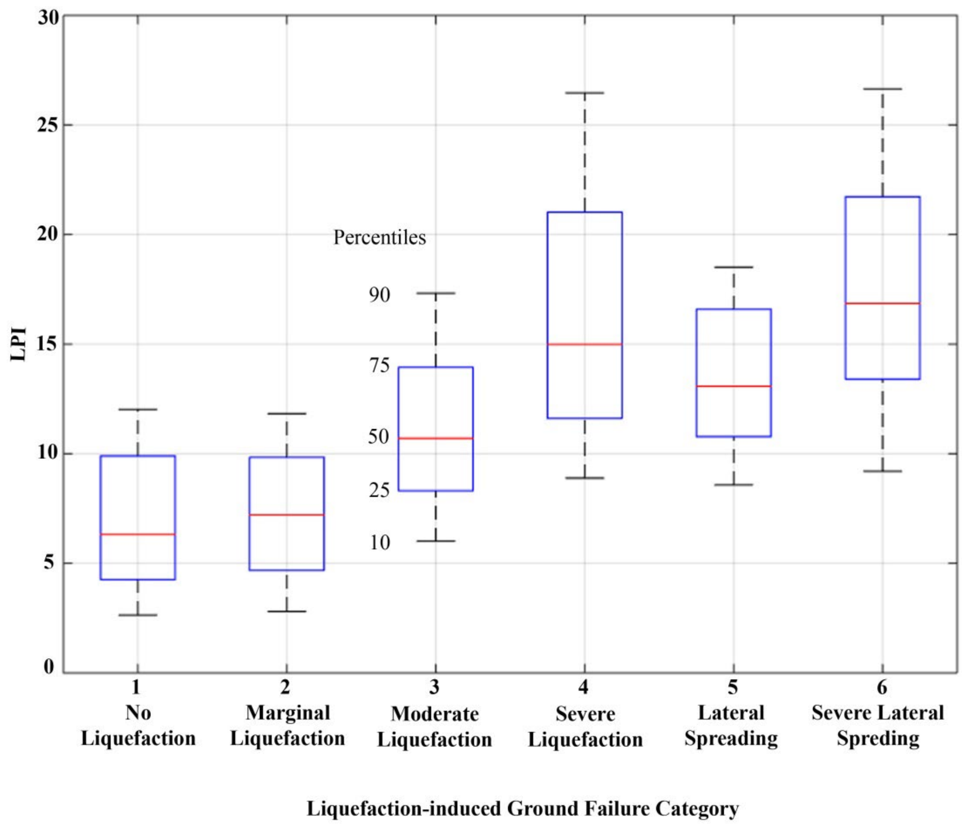
30
25
20
15
10
5
0
LPI
Percentiles
90
75
50
25
10
1
No Liquefaction
2
Marginal Liquefaction
3
Moderate Liquefaction
4
Severe Liquefaction
5
Lateral Spreading
6
Severe Lateral Spreding
Liquefaction-induced Ground Failure Category

Figure 7

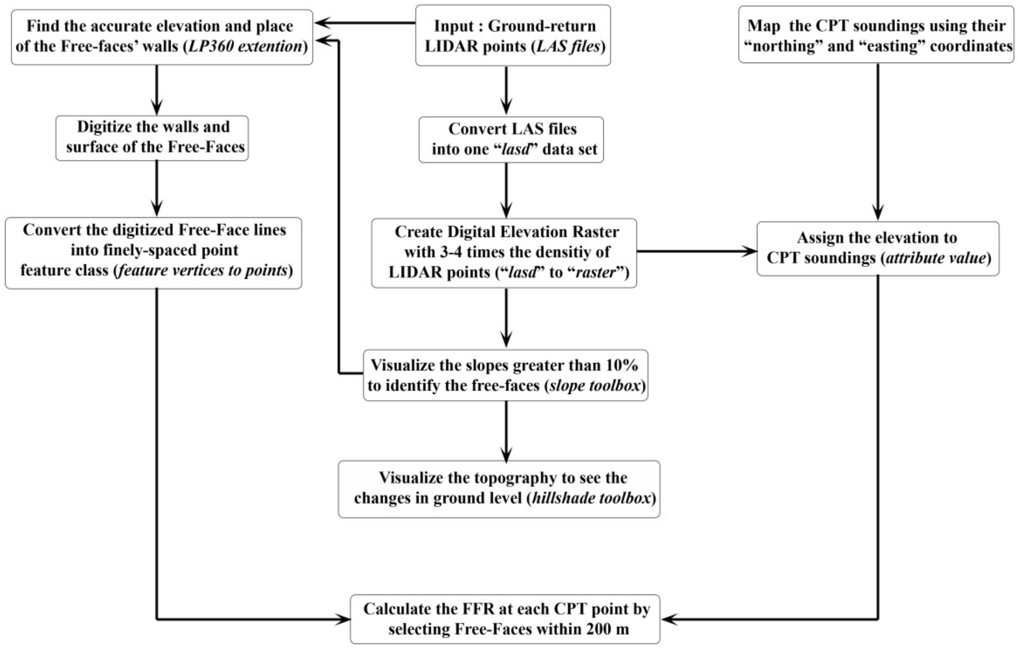
Find the accurate elevation and place of the Free-faces' walls (LP360 extention)
Input : Ground-return LIDAR points (LAS files)
Map the CPT soundings using their "northing" and "easting" coordinates
Digitize the walls and surface of the Free-Faces
Convert LAS files into one "lasd" data set
Convert the digitized Free-Face lines into finely-spaced point feature class (feature vertices to points)
Create Digital Elevation Raster with 3-4 times the densitiy of LIDAR points ("lasd" to "raster")
Assign the elevation to CPT soundings (attribute value)
Visualize the slopes greater than 10% to identify the free-faces (slope toolbox)
Visualize the topography to see the changes in ground level (hillshade toolbox)
Calculate the FFR at each CPT point by selecting Free-Faces within 200 m

Figure 8

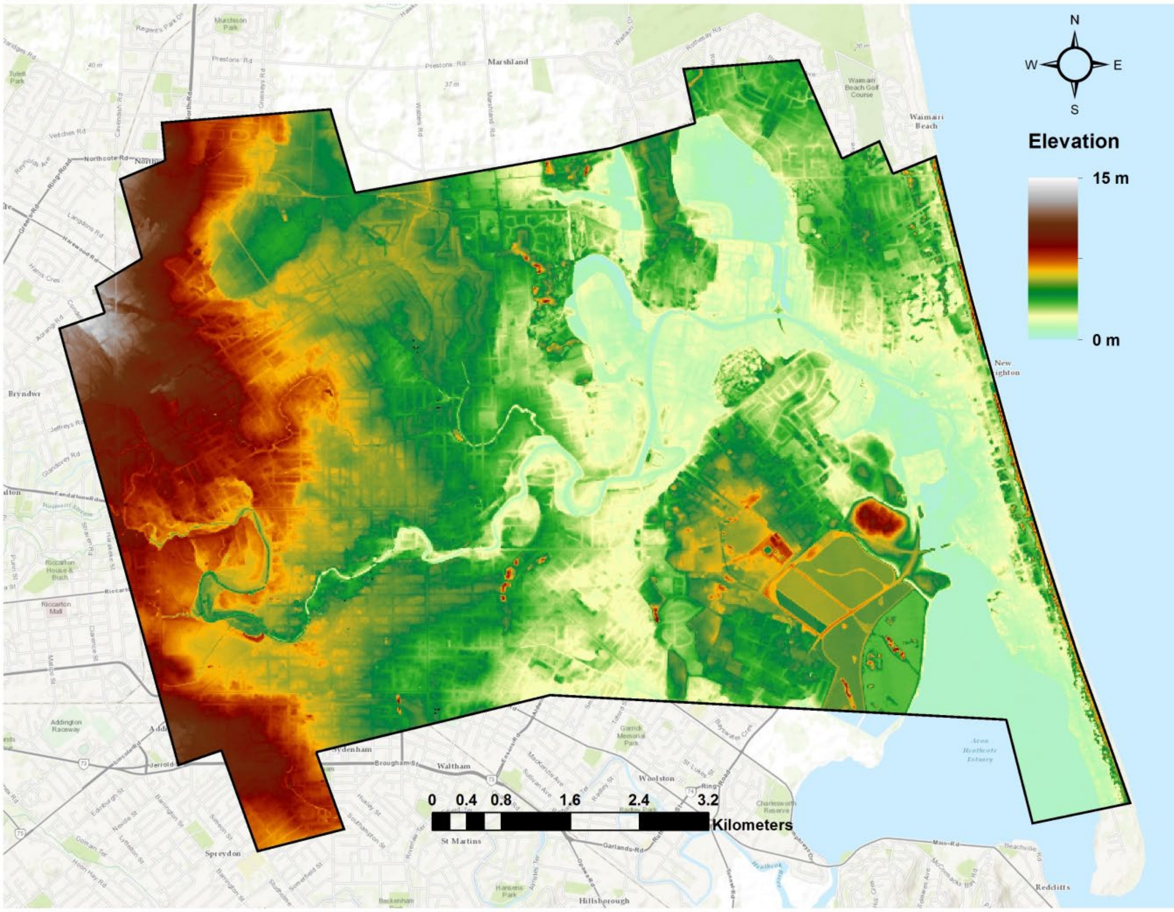

Figure 9

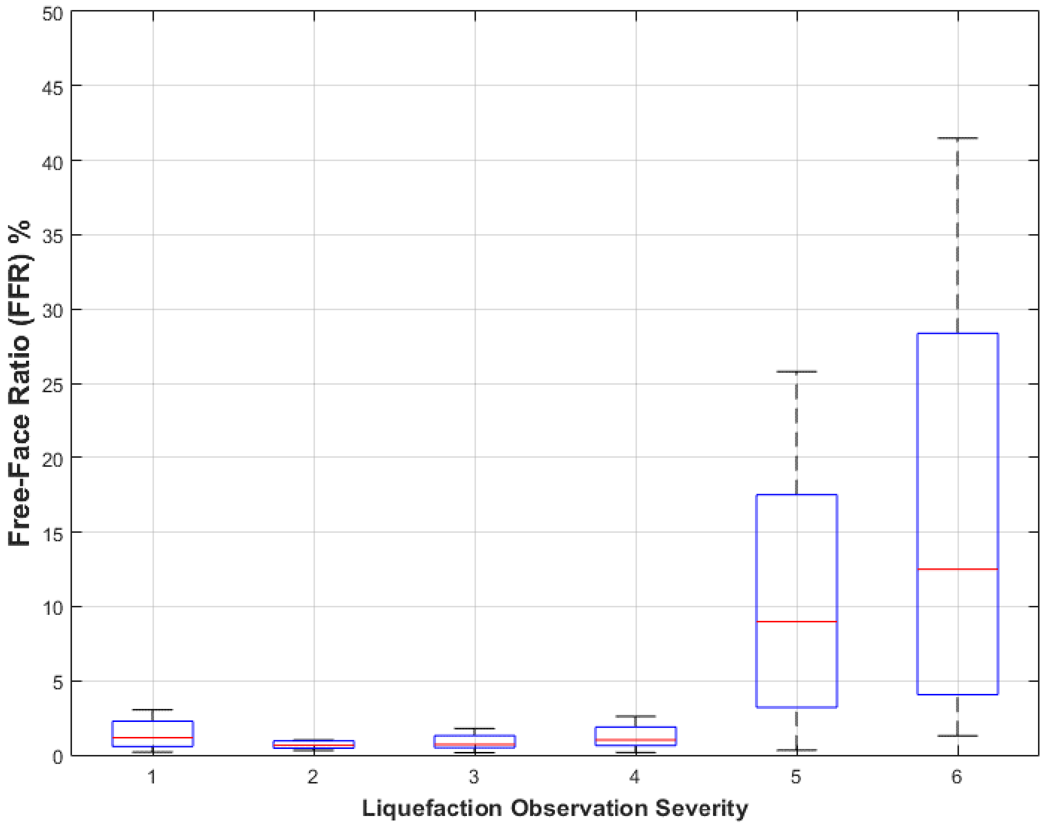
Free-Face Ratio (FFR) %
Liquefaction Observation Severity
0
5
10
15
20
25
30
35
40
45
50
1
2
3
4
5
6

Figure 10

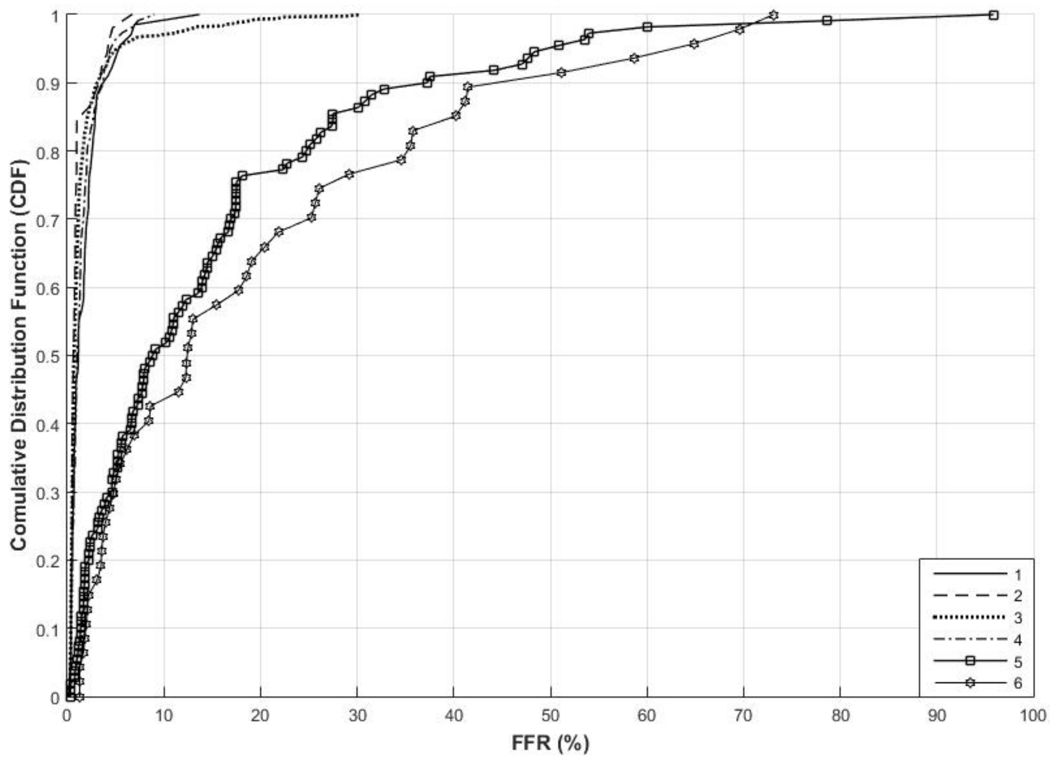

Figure 11

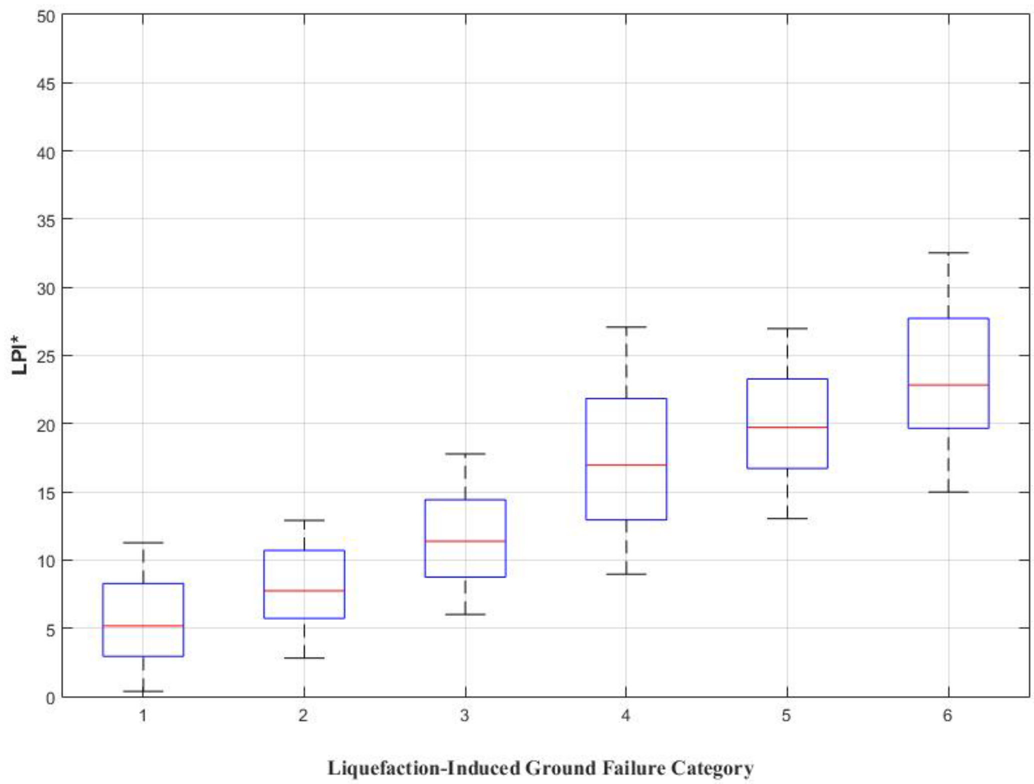
50
45
40
35
30
25
20
15
10
5
0
LPI*
1
2
3
4
5
6
Liquefaction-Induced Ground Failure Category

Figure 12

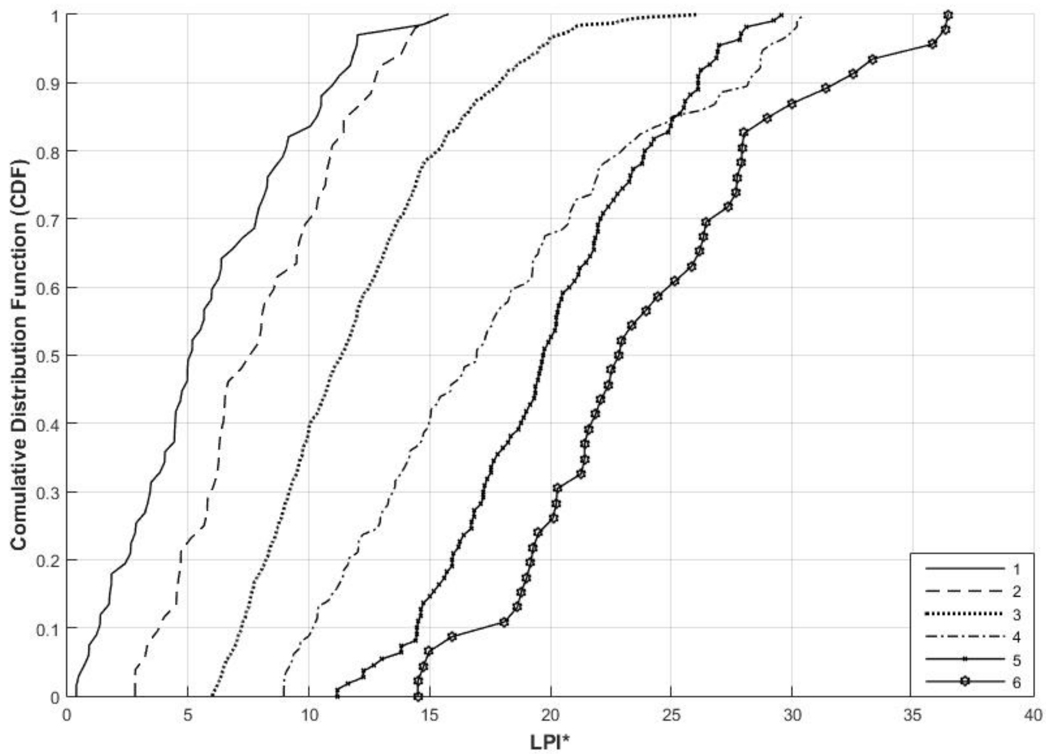

Figure 13

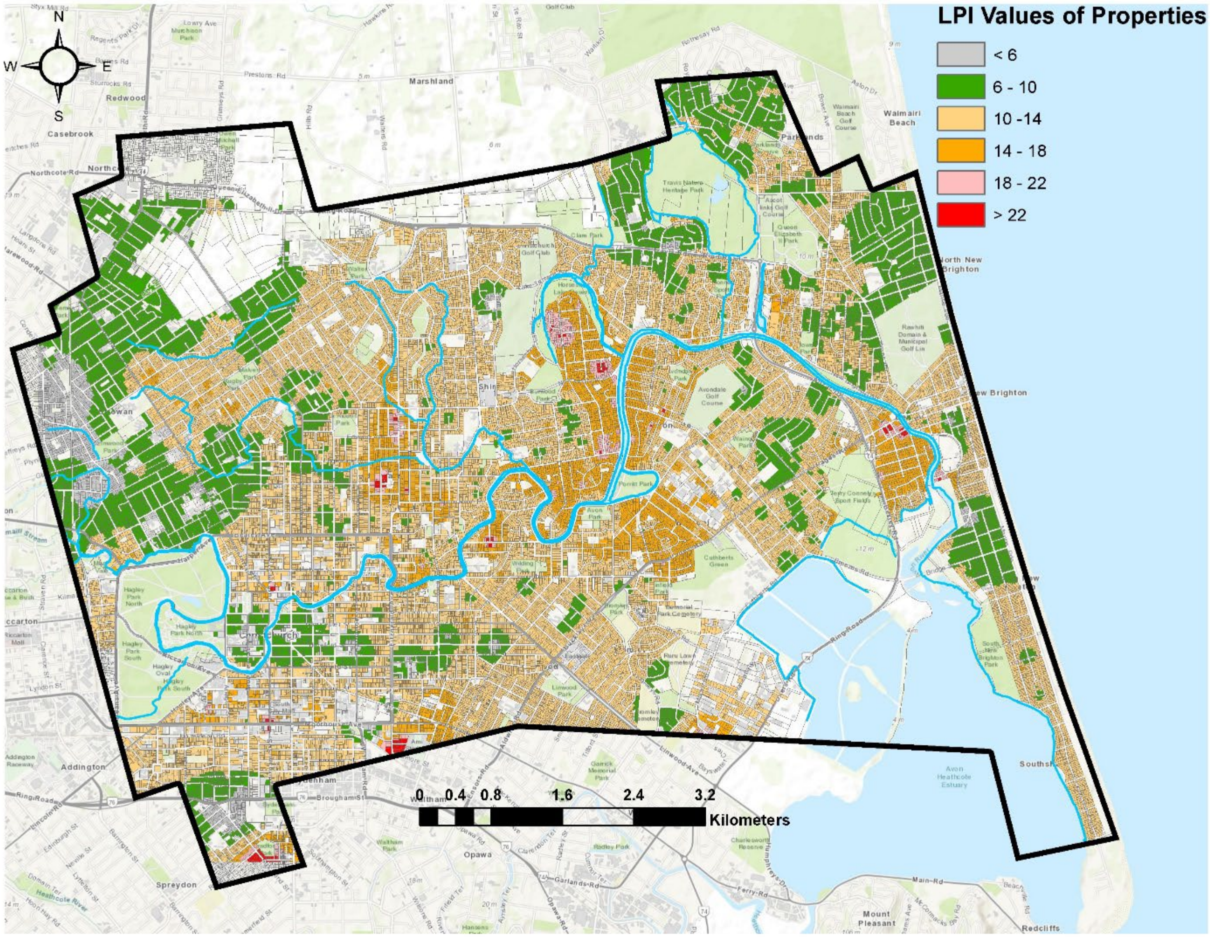
LPI Values of Properties
< 6
6 - 10
10 -14
14 - 18
18 - 22
> 22
N
S
E
W
0
0.4
0.8
1.6
2.4
3.2
Kilometers

Figure 14

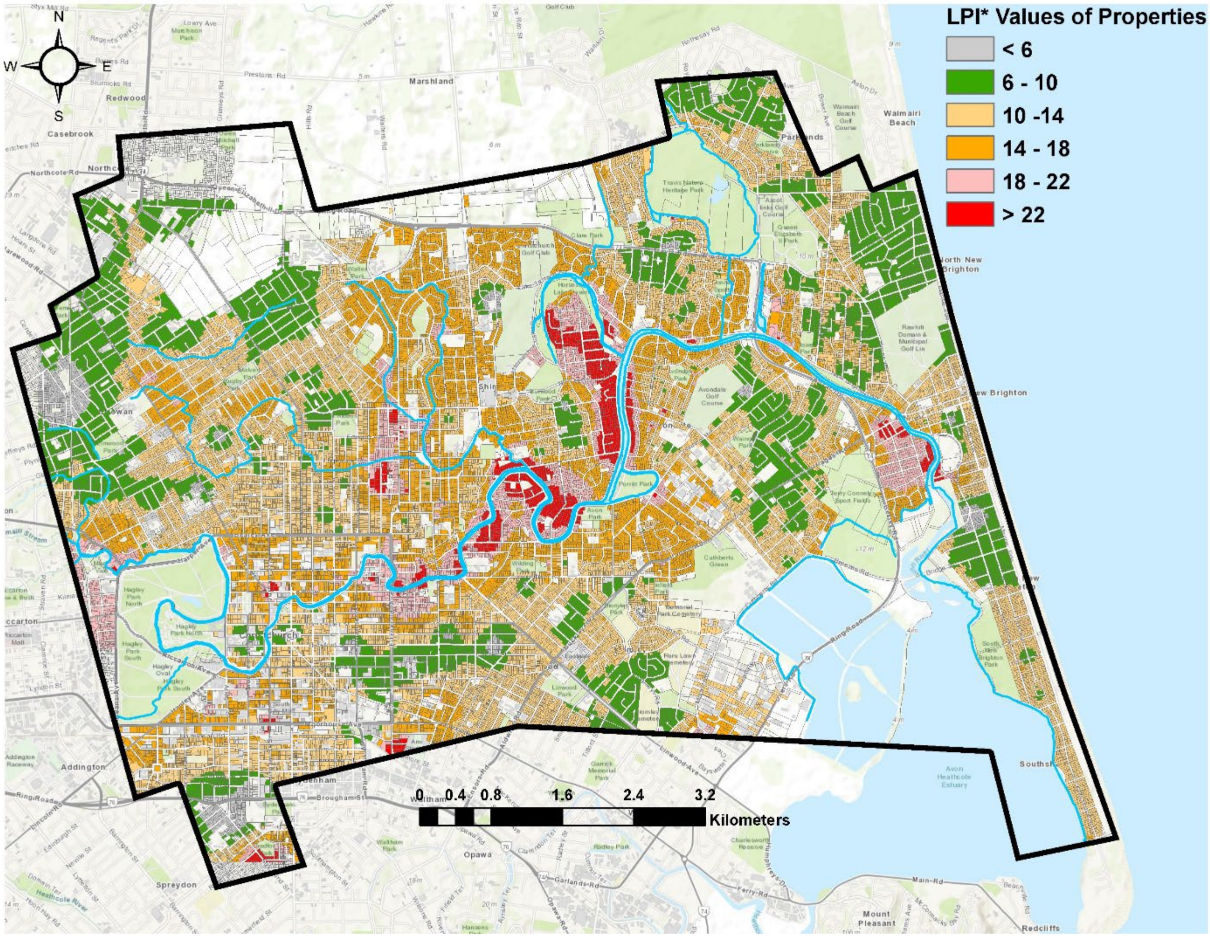

LPI* Values of Properties
< 6
6 - 10
10 -14
14 - 18
18 - 22
> 22
N
W
E
S
0
0.4
0.8
1.6
2.4
3.2
Kilometers

Figure 15

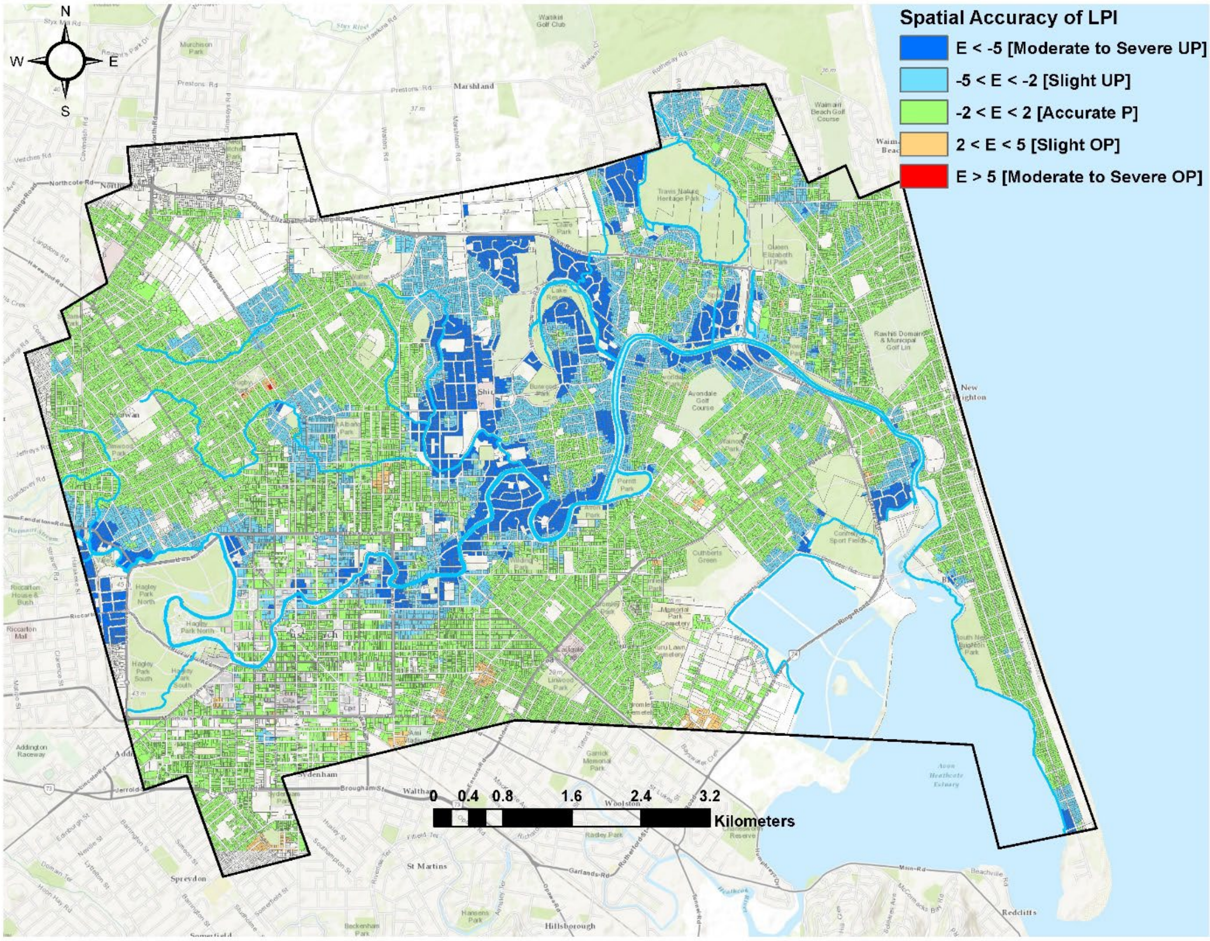
Spatial Accuracy of LPI
E < -5 [Moderate to Severe UP]
-5 < E < -2 [Slight UP]
-2 < E < 2 [Accurate P]
2 < E < 5 [Slight OP]
E > 5 [Moderate to Severe OP]
N
S
W
E
0 0.4 0.8 1.6 2.4 3.2
Kilometers

Figure 16

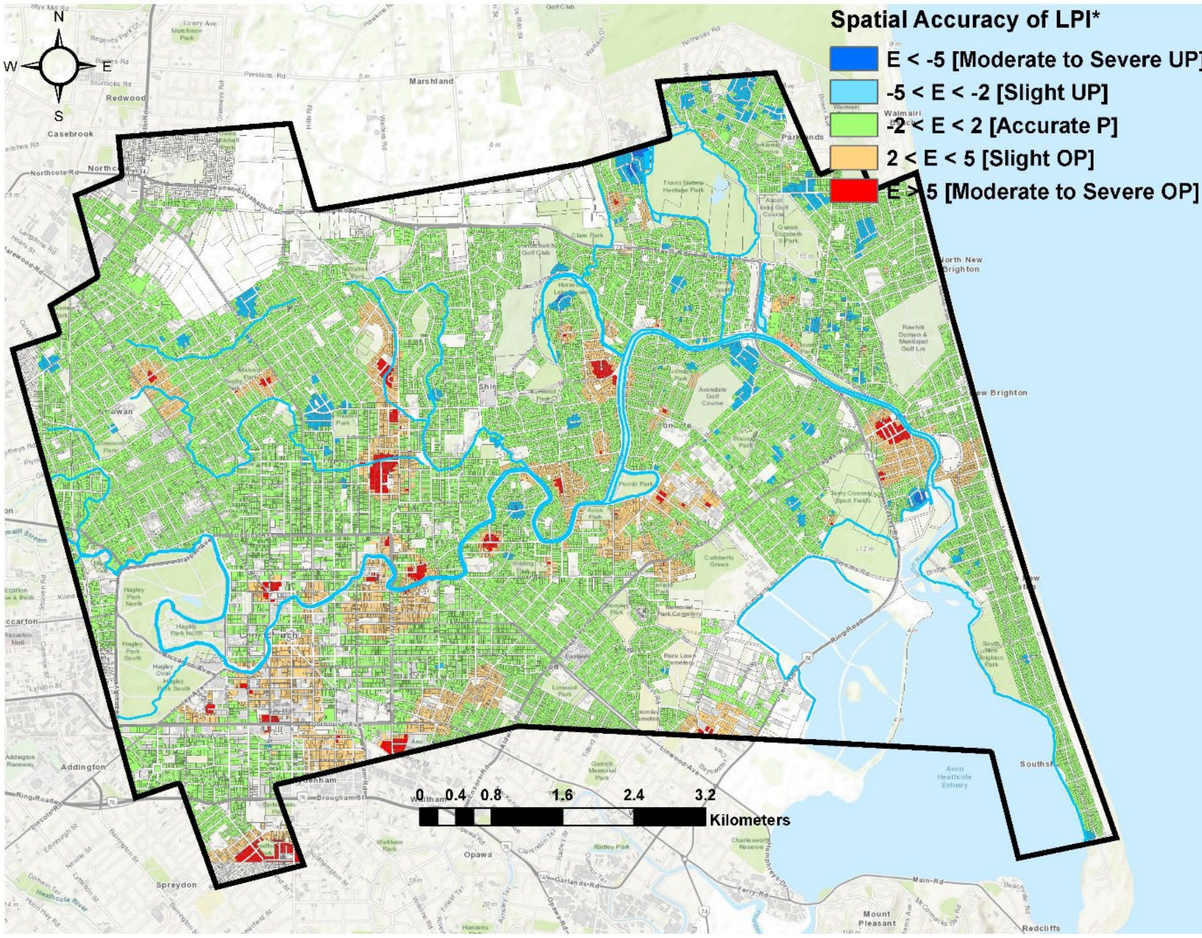
Spatial Accuracy of LPI*
E < -5 [Moderate to Severe UP]
-5 < E < -2 [Slight UP]
-2 < E < 2 [Accurate P]
2 < E < 5 [Slight OP]
E > 5 [Moderate to Severe OP]
N
E
S
W
0 0.4 0.8 1.6 2.4 3.2
Kilometers